CELL BIOLOGY

Dynein-dependent positioning of multiple organelles regulates adaptive gene expression during oxidative stress

Lucas Albacete-Albacete*, Li Jin, Nanami Sato, Marta N. Shahbazi, Simon L. Bullock*

Copyright © 2026 The Authors, some rights reserved; exclusive licensee American Association for the Advancement of Science. No claim to original U.S. Government Works. Distributed under a Creative Commons Attribution License 4.0 (CC BY).

Cells respond to environmental insults through well-characterized changes to their transcriptome and proteome. The contribution that reorganization of intracellular architecture makes to the adaptive stress response is much less understood. Here, we reveal a conserved spatial response to oxidative stress in which the microtubule motor dynein enhances perinuclear clustering of multiple membrane-bound organelles. These events are triggered by reactive oxygen species and protein kinase C and occur without increased association of dynein with its activator dynactin, pointing to a noncanonical mechanism for stimulating retrograde transport. Using a chemically inducible system for dispersing individual organelles, we show that perinuclear localization of multiple compartments potentiates oxidative stress–induced gene expression, with distinct genes depending on inputs from either combinations of organelles or individual compartments. Together, these findings implicate positioning of multiple membrane-bound compartments in gene expression regulation and identify coordinated organelle trafficking by dynein as an additional regulatory layer in the cellular stress response.

INTRODUCTION

Cells must contend with environmental fluctuations that challenge their integrity and homeostasis. External factors—including oxidative stress, nutrient deprivation, hypoxia, and inflammatory signals—can compromise essential cellular functions by damaging macromolecules and membranes. To cope with these insults, cells activate stress response pathways that trigger extensive reprogramming of their transcriptome and proteome, as well as metabolic rewiring (*1*, *2*). These processes are orchestrated by multiple stress-associated kinases, which integrate environment cues and relay them to effectors of the adaptive response.

In addition to these alterations, stress can trigger the formation of membraneless biomolecular condensates including stress granules and processing bodies in the cytoplasm and paraspeckles and PML bodies in the nucleus (*3*–*5*). Although these structures are a conserved feature of stress responses, their functional contribution to cellular adaptation remains debated (*6*–*8*). Comparatively little attention has been paid to how stress influences the location of membrane-bound organelles. However, there are reports that lysosomes can be repositioned by inflammatory (*9*) and metabolic cues (*10*, *11*) and that the distribution of mitochondria is sensitive to hypoxia and heat shock (*12*, *13*). While these observations point to a potential link between cellular stress and subcellular organelle localization, the extent to which cells reposition their membrane-bound compartments in response to insults is not known. Moreover, the molecular mechanisms that underpin stress-induced organelle relocalization, as well as the functional outputs of this process, are not clear.

Here, we demonstrate that oxidative stress stimulates retrograde transport of multiple organelles by the microtubule motor dynein, resulting in their clustering in the vicinity of the nucleus. We show that this process, which we refer to as stress-induced perinuclear organelle transport (SPOT), uses a noncanonical mechanism for stimulating dynein activity that is mediated by reactive oxygen species (ROS) and protein kinase C (PKC). Using a selective dispersal system in stressed cells, we demonstrate that perinuclear organelle positioning stimulates expression of genes associated with the adaptive response. Further, we show that activation of distinct genes is modulated by combinatorial or individual effects of specific organelles in the perinuclear region. Together, our findings reveal that reprogramming of gene expression in response to oxidative stress is facilitated by coordinated trafficking of multiple membrane-bound compartments by dynein.

Division of Cell Biology, MRC Laboratory of Molecular Biology, Cambridge, UK.
*Corresponding author. Email: lalbacete@mrclmb.ac.uk (L.A.-A.); sbullock@mrclmb.ac.uk (S.L.B.)

RESULTS

Oxidative stress repositions multiple organelles in the perinuclear region of cells

To determine the extent to which cells relocalize membrane-bound organelles in response to stress, we used immunostaining to compare the distribution of lysosomes, the endoplasmic reticulum (ER), mitochondria, peroxisomes, recycling endosomes, and the Golgi apparatus between control U2OS cells and those treated with a commonly used oxidative stressor, sodium arsenite ($NaAsO_2$). These experiments used a 1-hour treatment with 300 μM arsenite, which was sufficient to induce formation of stress granules (fig. S1A). Whereas the peroxisomes and the ER did not overtly change their distribution following arsenite addition (fig. S1A), this treatment enhanced the accumulation of lysosomes, mitochondria, recycling endosomes, and the Golgi in the perinuclear region of the cytoplasm (Fig. 1A). Time-lapse imaging revealed that increased perinuclear clustering of these organelles was evident within 10 min of arsenite addition and was completed ~40 min later (movies S1 to S4). Arsenite-induced redistribution of these organelles was not accompanied by changes in cell area (fig. S1B), indicating that this process involves active repositioning of the membrane-bound compartments rather than cell shrinkage.

We next examined the relative distribution of the repositioned organelles in the perinuclear region of arsenite-treated cells using multiplexed immunostaining. This approach demonstrated that lysosomes, recycling endosomes, and the Golgi became concentrated at a single perinuclear site, with the Golgi surrounding the other two organelles

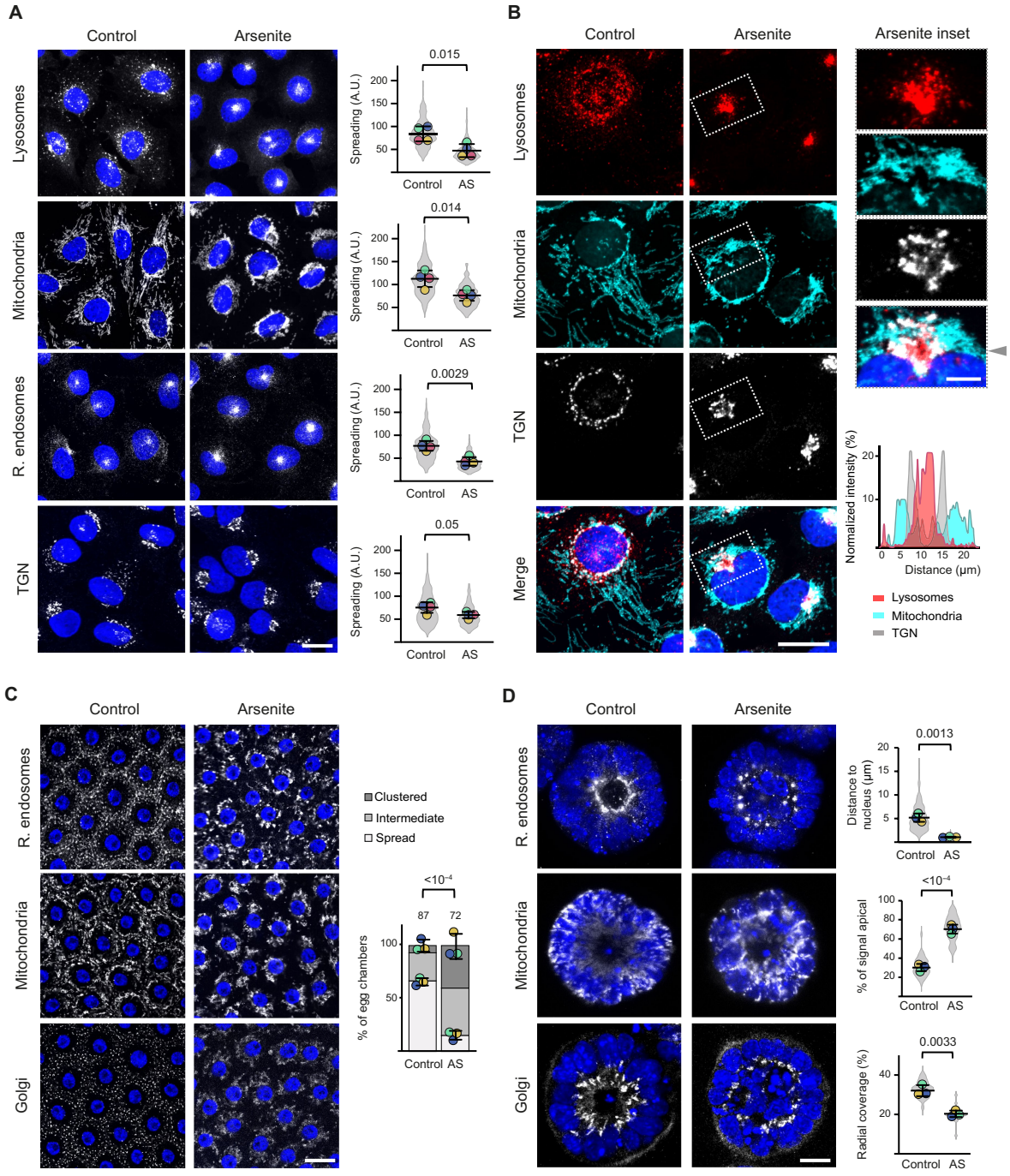

Fig. 1. Oxidative stress enhances perinuclear accumulation of multiple organelles. (**A**) Left: Confocal images of immunostained U2OS cells ± arsenite. Nuclei, blue [4′,6-diamidino-2-phenylindole (DAPI)]; organelles, grayscale [lysosomes (LAMP1), mitochondria (TOM20), recycling endosomes (r. endosomes; RAB11A), and trans-Golgi network (TGN; TGN46)]. Right: Quantification of organelle spreading. Violins display values for individual cells (>250 per condition). In this and other panels, circles show mean values per experiment ($N = 4$ in this case), and horizontal lines and error bars show means ± SD. A.U., arbitrary units; AS, arsenite. (**B**) Confocal images of immunostained U2OS cells ± arsenite [organelle markers as in (A)]. Chart shows line-scan analysis of organelle signal intensity across a profile extending horizontally from the arrowhead in the merged inset image. (**C** and **D**) Confocal images of organelle distribution in follicle cells of *Drosophila* egg chambers (C) or mouse ES cell (mESC)–derived spheroids (D) ± arsenite treatment. Nuclei, blue (DAPI); organelles, grayscale [(C) recycling endosomes (YFP-Rab11), mitochondria (ATP5A), and Golgi (GM130); (D) recycling endosomes (RAB11A), mitochondria (TOM20), and Golgi (GM130)]. In (C), chart shows categorization of organelle distribution. $N = 3$ experiments. Number of egg chambers examined shown above bars. In (D), charts show recycling endosome proximity to nucleus, apical distribution of mitochondria, and radial region from the lumen containing Golgi signal. Violins display per cell values for recycling endosomes and mitochondria (>100 per condition) or per spheroid values for Golgi (>25 per condition). $N = 3$ experiments. Scale bars, 20 μm [(A) and (B)], 5 μm [(B), inset)], or 40 μm [(C) and (D)]. Statistical significance was evaluated with Student's *t* test (two-tailed, unpaired) using mean values per experiment [(A) and (D)] or Fisher's exact test (C). *P* values shown above plots. One-hour treatment with 300 μM arsenite was used in all experiments.

(Fig. 1B and fig. S1C). In contrast, mitochondria condensed around most of the nucleus, reminiscent of the pattern observed under hypoxic and heat shock conditions (*12*, *13*). In the region containing the other clustered organelles, the mitochondria were typically peripheral to the Golgi (Fig. 1B), resulting in a multilayered organelle structure (fig. S1D). Thus, U2OS cells respond to arsenite by coordinately redirecting a subset of organelles to the perinuclear region. This process was reversed when arsenite was removed (fig. S1E), raising the possibility that it is part of the adaptive response to oxidative stress.

To determine whether perinuclear organelle clustering is a generalized response to oxidative insults, we investigated whether it occurs with other stressors, as well as in other cell types. We observed this phenomenon in U2OS cells in which oxidative stress was induced with hydrogen peroxide (H_2O_2) (fig. S2A) (*14*) or glucose deprivation (fig. S2B) (*15*, *16*), revealing that it is not specific to arsenite treatment. We also found that arsenite induced perinuclear clustering of organelles in two other immortalized human cell types examined—HeLa and RPE-1 (fig. S2, C and D)—as well as in squamous follicle cells of *Drosophila* egg chambers (Fig. 1C). In addition, arsenite triggered relocalization of organelles in polarized cystic spheroids formed by mouse embryonic stem (ES) cells (*17*). Following arsenite treatment of the spheroids, both the Golgi and recycling endosomes were redistributed within the apical cytoplasm, coalescing in a single spot adjacent to the nucleus, whereas mitochondria shifted from the basal cytoplasm to a diffuse apical distribution (Fig. 1D). Together, these observations reveal that relocalization of membrane-bound organelles occurs in response to several oxidative stressors, as well as in several cell types and organisms.

Stress-induced organelle repositioning is dependent on the dynein motor

We next investigated the mechanism by which organelles are clustered in the perinuclear region following oxidative stress. Cytoskeletal motors that run along actin or microtubule networks play a central role in organelle distribution. Whereas organelles are positioned along actin filaments by a single superfamily of myosin motors (*18*), their microtubule-based movements are mediated by two types of motors—dynein and kinesin—which move toward the minus or plus ends of their tracks, respectively (*19*, *20*). Dynein and kinesin frequently associate simultaneously with organelles, with the steady-state localization of the cargo determined by the frequency of movement of the two motor types (*21*).

To explore the role that transport by cytoskeletal motors plays in stress-induced organelle redistribution, we pharmacologically perturbed the microtubule or actin networks in arsenite-treated U2OS cells. Depletion (cytochalasin D) or stabilization (jasplakinolide) of the actin cytoskeleton did not affect perinuclear clustering of organelles (fig. S3). In contrast, disruption of microtubules with nocodazole resulted in strong dispersion of organelles (fig. S4A). Thus, clustering of organelles near the nucleus in stressed cells is dependent on an intact microtubule cytoskeleton.

There were no overt changes in the architecture of the microtubule network in arsenite-treated cells (fig. S4B), suggesting that organelle repositioning stems from alterations to the behavior of transport complexes rather than to the tracks along which they move. Dynein is a strong candidate to be the motor responsible for stress-induced organelle relocalization, as the perinuclearly positioned centrosome is the major site of microtubule minus end nucleation (*22*). Supporting this notion, the multiorganelle cluster in stressed cells was centered on the centrosome (fig. S5A). Moreover, the centrosomal enrichment of DCTN1 (*23*), a subunit of dynein's activator dynactin, was significantly increased by arsenite treatment (Fig. 2A and fig. S5A). We also observed arsenite-induced accumulation of a major kinesin motor, KIF5B, at the centrosome (fig. S5B). This observation is consistent with arsenite redirecting cargoes that simultaneously bind dynein and kinesin to the perinuclear region by increasing the relative frequency of dynein-based movements.

To directly test whether dynein is responsible for perinuclear organelle relocalization in stressed cells, we depleted its heavy chain (DYNC1H1) or its activator lissencephaly-1 (LIS1) by small interfering RNA (siRNA). Both treatments dispersed lysosomes, recycling endosomes, mitochondria, and the Golgi from the perinuclear region of arsenite-treated cells (Fig. 2B). Collectively, these data reveal that oxidative stress stimulates clustering of multiple organelles in the perinuclear region of the cell via a dynein-dependent process. Therefore, we refer to this phenomenon as stress-induced perinuclear organelle transport (SPOT).

We next turned our attention to how dynein-based trafficking of organelles is influenced by oxidative stress. The canonical mechanism of dynein activation is through recruitment of dynactin (Fig. 2C) (*24*, *25*). This regulatory strategy is used by cargo-associated coiled-coil proteins (so called "activating adaptors") and LIS1, which promote assembly of the dynein-dynactin complex and thereby enhance the frequency, velocity, and duration of transport events (*26*–*29*). To determine whether oxidative stress increases the interaction of dynein with dynactin, we used a green fluorescent protein (GFP)–tagged dynein subunit (DYNC1I2) to immunoprecipitate the motor complex from U2OS cells in the presence and absence of arsenite. The composition of the captured material was then analyzed using quantitative mass spectrometry. While the abundance of a number of proteins in GFP-dynein immunoprecipitates was affected by arsenite (fig. S6A), the abundance of dynactin components was not altered (Fig. 2D). This result was confirmed by analysis of captured material with immunoblotting (Fig. 2E). Arsenite also did not alter the association of dynein with LIS1 (fig. S6B) or the prototypical activating adaptor, BICD2 (fig. S6, C and D).

These data suggest that oxidative stress does not stimulate retrograde organelle transport by promoting the formation of the dynein-dynactin complex. Notably, while the association of dynein with dynactin, LIS1, and BICD2 was not affected by arsenite, we consistently observed arsenite-induced dissociation of dynein from another of its binding partners—NDEL1 (Fig. 2E). Reduction in dynein's association with NDEL1 was evident within 15 min of arsenite treatment and was therefore temporally aligned with the initiation of organelle relocalization (movies S1 to S4 and fig. S7A). Impaired association of dynein with NDEL1 was also observed after SPOT was triggered with H_2O_2 or glucose deprivation (fig. S7, B and C). Together, these data implicate the dynein-NDEL1 interaction as a potential regulatory node in stress-induced organelle repositioning.

SPOT requires ROS formation and is activated by PKC

We next investigated the processes that are upstream of activation of dynein-based organelle transport in stressed cells. While oxidative stress is most commonly mediated by ROS, other factors—including metabolite imbalance and mitochondrial dysfunction—can also play a role (*30*–*33*). We found that the antioxidant *N*-acetyl-L-cysteine suppressed arsenite-induced perinuclear organelle clustering (fig. S8A),

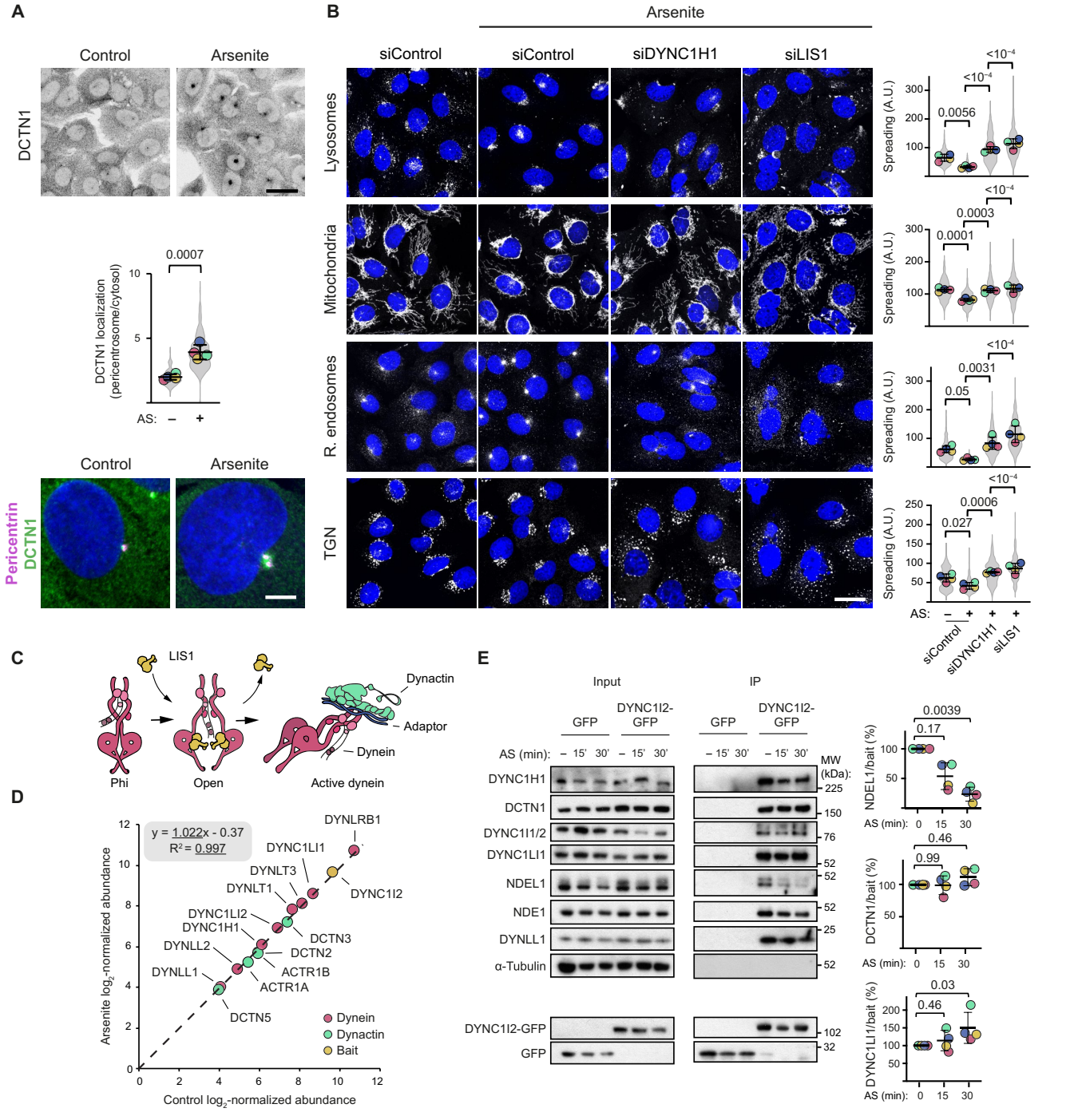

Fig. 2. Stress-induced organelle repositioning requires dynein. (**A**) Confocal images of dynactin (DCTN1) in control (untreated) and arsenite-treated (300 μM, 1 hour) cells without (top) (signal in inverted grayscale) and with (bottom) costaining for the centrosomal marker pericentrin [nuclei, blue (DAPI)]. Violins display values for DCTN1 localization from individual cells (>250 per condition). (**B**) Left: Confocal images of U2OS cells ± arsenite (300 μM, 1 hour) after 72 hours of treatment with indicated siRNA pools (siControl, nontargeting pool). Nuclei, blue (DAPI); organelles, grayscale [lysosomes (LAMP1), mitochondria (TOM20), recycling endosomes (RAB11A), and TGN (TGN46)]. Right: Quantification of organelle spreading. Violins display values for individual cells (>250 per condition). (**C**) Schematic of canonical model of dynein activation. (**D**) Scatter plot of abundance of dynein (red) or dynactin (green) subunits or bait (yellow) in GFP immunoprecipitates from untreated (control) or arsenite-treated (300 μM, 30 min) DYNC1I2-GFP U2OS cells. Datapoints are mean values from three independent experiments. (**E**) Immunoblot analysis of indicated proteins in GFP immunoprecipitates from GFP or DYNC1I2-GFP cells treated with 300 μM arsenite for indicated times. α-Tubulin is a negative control showing specificity of the immunoprecipitation (IP). Charts show normalized ratio of immunoblot signals of indicated proteins to those of DYNC1I2-GFP. In (A), (B), and (E), circles show mean values [(A) and (B)] or individual values (E) per experiment ($N = 4$), and horizontal lines and error bars show means ± SD. Scale bars, 20 μm [(A), top], 5 μm [(A), bottom], or 20 μm (B). Statistical significance was evaluated with Student's *t* test (two-tailed, unpaired) (A) or a one-way analysis of variance (ANOVA) with Dunnett's multiple comparisons test [(B) and (E)] using mean values per experiment [(A) and (B)] or per experiment values (E). *P* values are shown above plots. MW, molecular weight.

revealing that ROS is a key driver of this process. Preventing the formation of ROS with *N*-acetyl-L-cysteine also significantly impaired the release of NDEL1 from dynein without affecting the dynein-dynactin interaction (fig. S8B), consistent with a link between NDEL1 dissociation and SPOT.

ROS acts not only as a damaging agent but also as a signaling molecule, activating multiple kinase pathways that regulate adaptive responses to stress (*34*, *35*). To probe the molecular events that connect ROS to SPOT, we incubated arsenite-treated cells with inhibitors of 13 known stress-associated kinases and determined the effects on localization of lysosomes, mitochondria, recycling endosomes, and the Golgi (Fig. 3A and fig. S9, A and B). While some inhibitors impaired perinuclear clustering of specific organelles, only those inhibitors targeting PKC (sotrastaurin) or the mitogen-activated protein kinase p38 (PD169316) led to dispersal of each of them. These effects of sotrastaurin and PD169316 on organelle relocalization were confirmed in multiple additional experiments (Fig. 3B and fig. S10). We also found that a second PKC inhibitor (Gö6983), as well as a pool of siRNAs targeting multiple PKC isoforms, impaired arsenite-induced clustering of lysosomes, mitochondria, the Golgi, and recycling endosomes (fig. S11, A and B).

The above results indicated that PKC and p38 are critical for SPOT. To test whether PKC or p38 inhibitors prevent SPOT indirectly by affecting the integrity or organization of the microtubule network, we stained treated cells with an antibody to α-tubulin. The p38 inhibitor caused disorganization of the microtubule network, with abnormal bundling of filaments around the nucleus (fig. S12A), offering an explanation for why it prevents SPOT. In contrast, no overt changes in the microtubule network were seen with PKC inhibition (fig. S12A). This observation raised the possibility that PKC directly promotes retrograde organelle transport in response to oxidative stress. Supporting this notion, sotrastaurin prevented the arsenite-induced increase in centrosomal localization of DCTN1 and KIF5B (fig. S12B). Moreover, unlike the p38 inhibitor, it also impaired release of NDEL1 from dynein (Fig. 3C). This effect was not accompanied by a change in the interaction of dynactin with dynein (fig. S12C). To test whether PKC activation is sufficient to stimulate perinuclear localization of organelles, we treated cells with phorbol 12-myristate 13-acetate (PMA), which activates PKC by mimicking the natural ligand diacylglycerol (*36*). Notably, in the absence of arsenite, PMA treatment was sufficient to recapitulate enhanced perinuclear organelle clustering (Fig. 3D), as well as the release of NDEL1 from dynein (fig. S12D). Collectively, these results demonstrate that PKC activation is a key driver of retrograde organelle transport in response to oxidative stress.

Dynein-based transport augments oxidative stress–responsive gene expression

Our observation that enhanced perinuclear clustering of multiple organelles is a conserved response to oxidative stress across cell types and species supports a role for this process in stress adaptation. As organelles have been proposed to act as signaling platforms that modulate gene expression programs in the nucleus (*37*–*41*), we hypothesized that SPOT influences oxidative stress–induced transcriptional reprogramming (*35*, *42*).

To test this notion, we first used RNA sequencing (RNA-seq) to identify arsenite-induced genes in U2OS cells. A total of 587 mRNAs were more abundant in cells treated with arsenite for 2 hours than in untreated control cells [fig. S13A; $\log_2$ fold increase of >0.58 and false discovery rate (FDR) of <0.05]. The most up-regulated of these genes (31 with a $\log_2$ fold increase of >2.5) included several that encode proteins with functions related to proteostasis (9 genes) or cellular detoxification (3 genes) or that are stress-responsive transcriptional regulators (9 genes) (fig. S13, A and B). These functional categories were previously found to be up-regulated in response to arsenite in human skin fibroblasts (*43*) and comprised genes that are well known transcriptional targets of oxidative stressors (*44*, *45*).

We next prevented perinuclear localization of organelles in arsenite-treated cells by disrupting microtubules with nocodazole and compared the gene expression profile with that of arsenite-treated vehicle controls using RNA-seq. We found that 24 arsenite-responsive genes were less strongly induced in the presence of nocodazole (Fig. 4A; $\log_2$ fold decrease of >0.58 and FDR of <0.05). The expression of these genes under basal conditions was not reduced by nocodazole treatment (fig. S13C), revealing that only their induction by arsenite was altered by microtubule depolymerization. The 24 genes included several of those that were most strongly activated by arsenite when microtubules were intact (fig. S13A) and have functions related to proteostasis, including molecular chaperoning (Fig. 4B). Reverse transcription-quantitative polymerase chain reaction (RT-qPCR) validated the sensitivity of mRNAs in this category to nocodazole (Fig. 4C). This method additionally showed that several arsenite-responsive genes that were close to the cutoff for nocodazole sensitivity in the RNA-seq experiments consistently exhibited reduced induction by arsenite in the presence of nocodazole (fig. S14A). Genes in this category included several that encode transcriptional regulators of the stress response (*46*, *47*). Moreover, we showed using immunoblotting and immunofluorescence that the observed reductions in arsenite-induced mRNAs in nocodazole-treated cells were reflected in impaired expression of protein products (Fig. 4D and fig. S14B).

If the ability of nocodazole to impair arsenite-induced gene expression reflects perturbation of perinuclear organelle accumulation, rather than a transport-independent function of microtubules, similar effects should be seen when the dynein motor is perturbed. To test whether this is the case, we knocked down DYNC1H1 in arsenite-treated cells (Fig. 4E) and used RT-qPCR to monitor expression of stress-responsive mRNAs that are nocodazole sensitive. Depletion of DYNC1H1 significantly reduced the induction of these genes by arsenite (Fig. 4E and fig. S14C), consistent with a role for retrograde organelle transport in this process. Further supporting this notion, inhibition of PKC with sotrastaurin similarly impaired the induction of this set of genes (Fig. 4F and fig. S14D). Thus, we find that multiple independent methods of perturbing SPOT compromise transcriptional reprogramming in arsenite-treated cells, including efficient induction of genes involved in proteostasis. These data support a link between PKC-mediated activation of retrograde transport and oxidative stress–induced remodeling of gene expression.

To evaluate the potential functional implications of the gene expression changes observed when SPOT is disrupted, we assessed the consequences of acutely disrupting microtubules on the response of cells to an oxidative insult. Impaired proteostasis, including defects in molecular chaperone function, can compromise the clearance of misfolded and damaged proteins, leading to the accumulation of ubiquitinated species (*48*, *49*). We therefore examined the abundance of ubiquitinated proteins in cells recovering from transient exposure to arsenite (2, 4, or 6 hours) in the presence and absence of nocodazole (fig. S15A). Immunoblotting of cell extracts 24 hours after washout of both compounds revealed higher levels of ubiquitinated proteins in cells treated with arsenite and nocodazole than in those treated

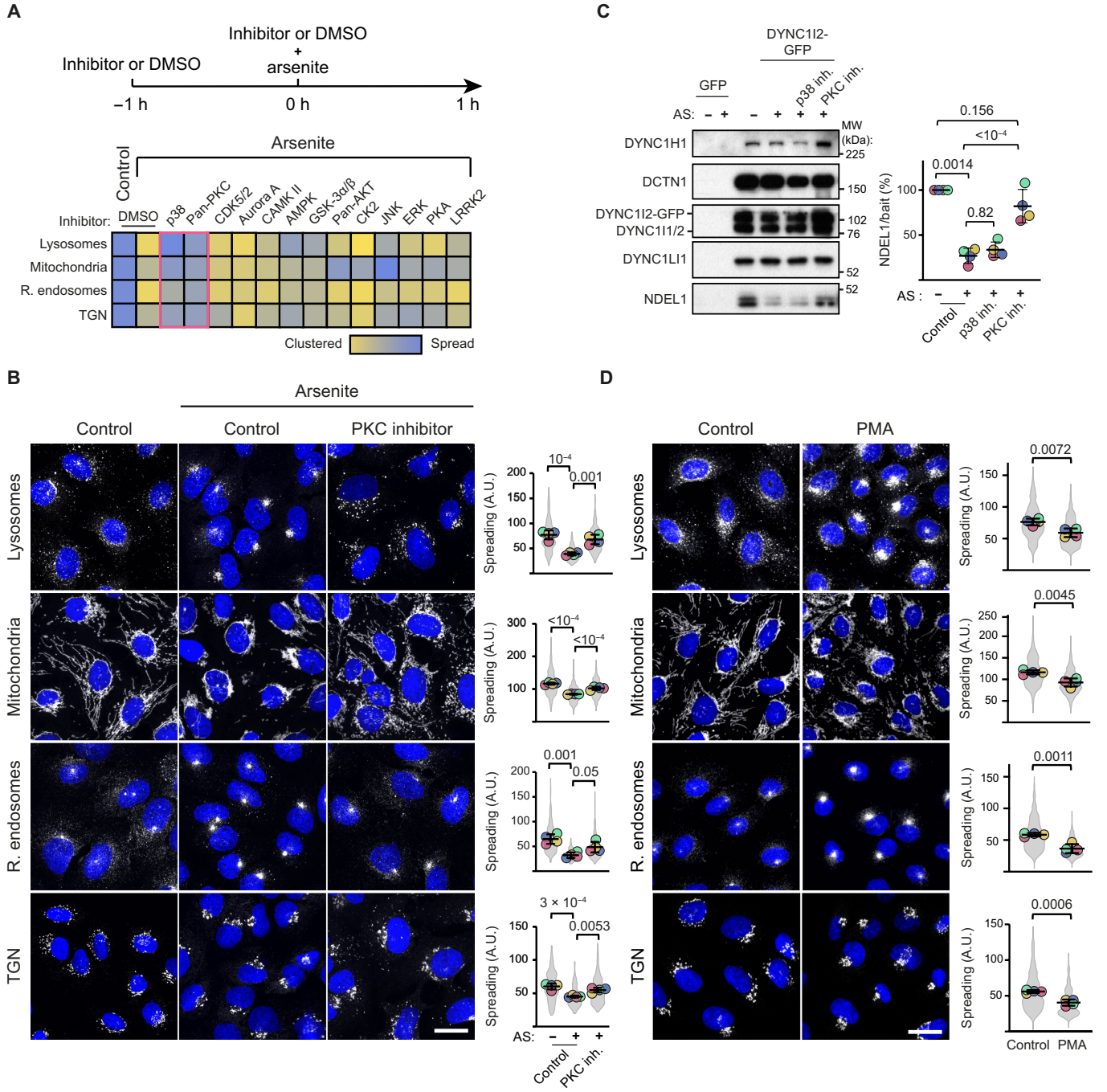

Fig. 3. PKC stimulates SPOT. (**A**) Kinase inhibition workflow. Dimethyl sulfoxide (DMSO; 0.1%), vehicle control. Heatmap shows minimum-maximum normalized spreading values (>100 cells per condition aggregated from two experiments). Inhibitors: p38, PD169316 (20 μM); pan-PKC, sotrastaurin (10 μM); CDK5/2, roscovitine (20 μM); Aurora A, TC-A 2317 hydrochloride (20 μM); calcium- and calmodulin-dependent protein kinase II (CAMKII), KN-62 (20 μM); AMPK, SBI-0206965 (20 μM); GSK-3α/β, SB216763 (20 μM); pan-AKT, ipatasertib (20 μM); CK2, silmitasertib (20 μM); c-Jun N-terminal kinase (JNK), SP600125 (20 μM); ERK, FR180204 (20 μM); PKA, KT5720 (10 μM); LRRK2, LRRK2-IN-1 (20 μM). Red box highlights p38 and PKC inhibition. (**B**) Left: Immunostained U2OS cells ± arsenite [300 μM, 1 hour (h)] in the absence (DMSO, control) or presence of sotrastaurin (10 μM). Nuclei, blue (DAPI); organelles, grayscale [lysosomes (LAMP1), mitochondria (TOM20), recycling endosomes (RAB11A), and TGN (TGN46)]. Right: Organelle spreading quantification. Violins show individual cell values (>250 per condition). inh., inhibitor. (**C**) Left: Immunoblots of indicated proteins in GFP or DYNC1I2-GFP immunoprecipitates from U2OS cells pretreated with vehicle (control), PD169316 (20 μM), or sotrastaurin (10 μM) for 1 hour before addition of 300 μM arsenite for 30 min. Right: Quantification of NDEL1 capture with DYNC1I2-GFP. (**D**) Left: Images of organelles in control (DMSO) or PMA-treated (10 μM, 1 hour) U2OS cells without arsenite [markers as in (B)]. Right: Organelle spreading quantification. Violins show individual cell values (>250 per condition). In (B) to (D), circles show mean values [(B) and (D)] and individual values (C) per experiment ($N = 4$); horizontal lines and error bars show means ± SD. Scale bars, 20 μm [(B) and (D)]. Statistical significance was evaluated with a one-way ANOVA with Dunnett's multiple comparisons test [(B) and (D)] or Student's *t* test (two-tailed, unpaired) (C) using mean values per experiment [(B) and (D)] or per experiment values (C). *P* values are shown above plots.

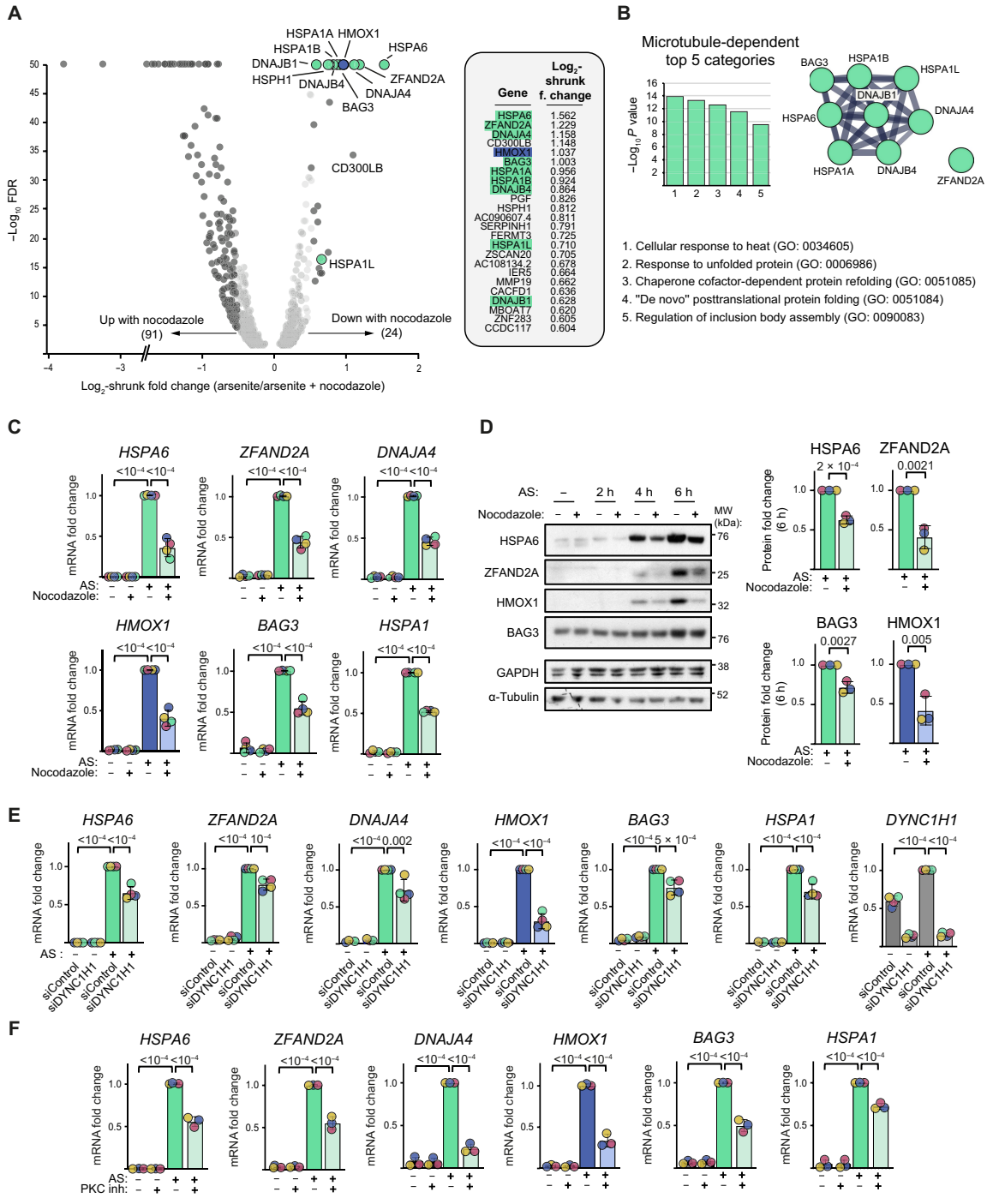

Fig. 4. Retrograde transport augments oxidative stress–induced gene expression. (**A**) RNA-seq–based analysis of U2OS cells pretreated with 10 μM nocodazole or vehicle (0.1% DMSO) for 1 hour, followed by addition of 150 μM arsenite for a further 2 hours. Genes with a $\log_2$-shrunk fold change of >0.58 (1.5-fold) are in dark gray, except for those in this category that are associated with proteostasis (green) or detoxification (blue). Inset shows 24 genes most affected by nocodazole. (**B**) Top 5 gene ontology (GO) categories associated with these 24 genes and STRING network analysis showing a proteostasis-associated functional cluster. (**C**) RT-qPCR–based validation of nocodazole's effect on arsenite-induced gene expression. In this panel, (E), and (F), circles show mean values of three technical replicates per experiment ($N = 4$), and horizontal lines and error bars show means ± SD. (**D**) Immunoblot analysis of lysates from U2OS cells treated with 150 μM arsenite for specified times in the absence (0.1% DMSO) or presence of 10 μM nocodazole (cells were preincubated with vehicle or nocodazole for 1 hour before arsenite addition). Charts show normalized expression of indicated proteins at 6 hours of treatment ($N = 3$ experiments). (**E** and **F**) RT-qPCR–based assessment of gene expression in U2OS cells treated with indicated siRNA pools (E) ($N = 4$ experiments) or 10 μM sotrastaurin (PKC inhibitor) or 0.1% DMSO (F) ($N = 3$ experiments), followed by addition of arsenite (150 μM for 2 hours). *DYNC1H1* mRNA levels were significantly reduced by siDYNC1H1, confirming knockdown. In (F), cells were pretreated for 1 hour with sotrastaurin or DMSO. Statistical significance was evaluated with a one-way ANOVA with Dunnett's multiple comparisons test [(C), (E), and (F)] or Student's *t* test (two-tailed, unpaired) (D) based on mean values per experiment. *P* values are shown above plots.

with arsenite alone (fig. S15B). Treatment with nocodazole alone did not affect the abundance of ubiquitinated species (fig. S15B). Thus, disrupting microtubules during an oxidative insult impairs restoration of protein homeostasis after the stressor is removed. In keeping with this finding, nocodazole-treated cells also exhibited increased cell death in the period following arsenite removal (fig. S15C). Together, these findings are consistent with a functional contribution of SPOT to proteostasis and cell survival following oxidative stress.

Distinct and combinatorial effects of organelle positioning on gene expression

The perturbations described above simultaneously disrupt perinuclear localization of several organelles. Therefore, they do not shed light on how the positioning of individual organelles influences stress-responsive changes in gene expression. To address this issue, we generated U2OS cell lines in which specific organelles can be excluded from the perinuclear region in stressed cells. This was achieved by tethering a constitutively active version of a plus-end-directed kinesin-1 motor (KIF5B) to organelles (Fig. 5A) (*50*), thereby counteracting their dynein-driven motion to the perinuclear region.

We produced cell lines in which the KIF5B motor can be inducibly recruited to mitochondria, lysosomes, recycling endosomes, or the Golgi using the rapalog-induced FKBP–FRB heterodimerization system (*51*) and specific organelle targeting sequences (Fig. 5A). In the absence of rapalog, the FKBP-rapamycin binding (FRB)-tagged organelles displayed their characteristic distributions in the presence and absence of arsenite (Fig. 5, B and C). Following rapalog addition without arsenite, ~50% of cells redistributed the targeted organelle

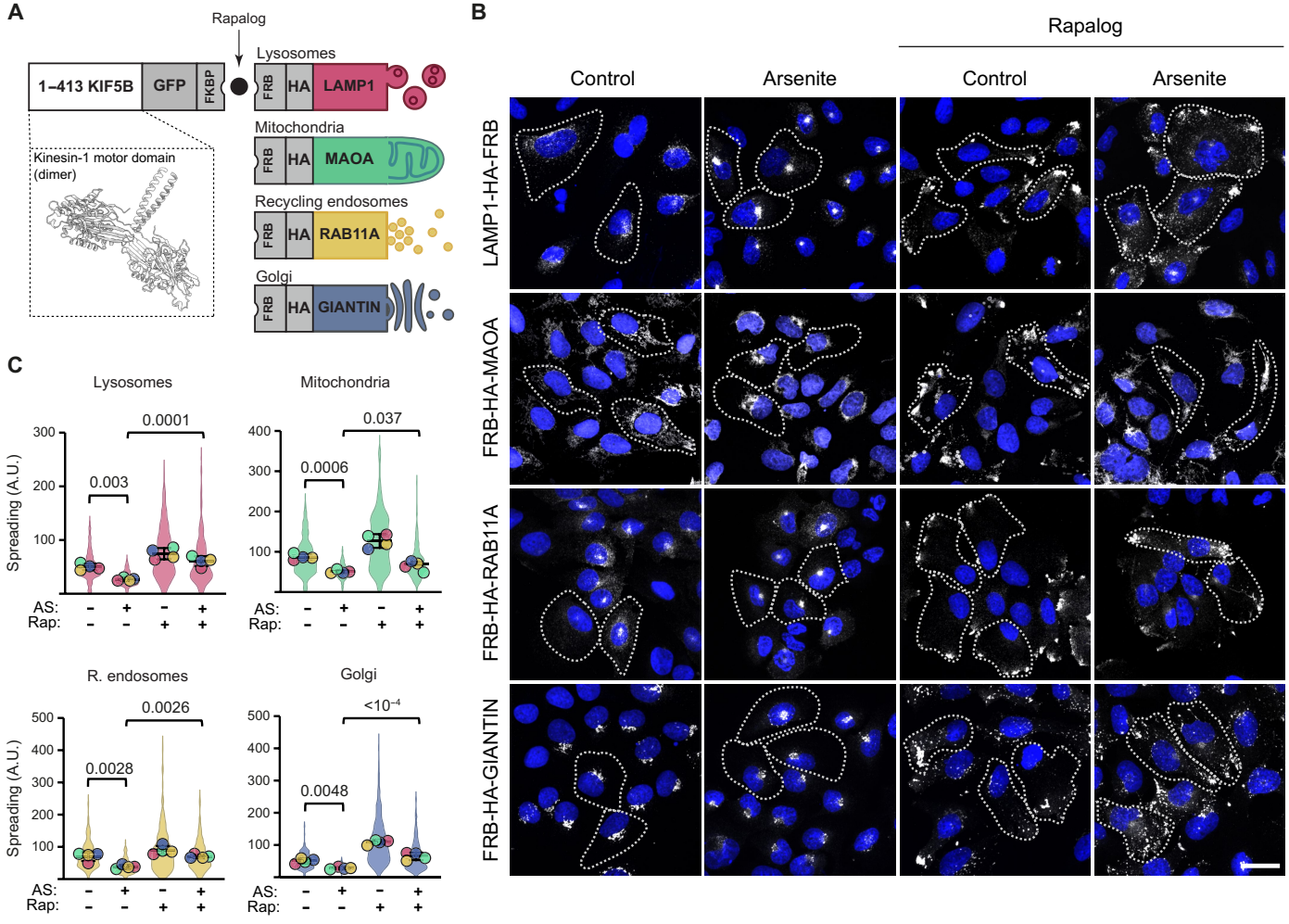

Fig. 5. An inducible system for dispersing individual organelles. (**A**) Schematic of rapalog-induced system for organelle dispersal. The FKBP domain is fused to the motor domain of KIF5B [amino acids 1 to 413, which form a homodimeric active motor (as shown in the structural rendering)], while the FRB domain is fused to the hemagglutinin (HA) epitope and the indicated organelle-specific targeting sequences. Each cell line expresses the KIF5B construct and a different organelle targeting construct. In the presence of rapalog, FKBP binds FRB to promote anterograde transport of the organelle of interest. (**B**) Confocal images of U2OS cells expressing KIF5B-GFP-FKBP and the indicated constructs that are untreated (control) or treated with 300 μM arsenite (4 hours) ± 10 nM rapalog (30-min rapalog pretreatment followed by treatment with rapalog and arsenite). Nuclei, blue (DAPI); organelles, grayscale (HA). Dashed lines show outlines of exemplar cells. Scale bar, 20 μm. (**C**) Quantification of organelle spreading in presence and absence of rapalog and arsenite. Violins display values per cell (>200 per condition). Circles show mean values per independent experiment ($N = 4$), and horizontal lines and error bars show means ± SD. Rap, rapalog. Statistical significance was evaluated with a one-way ANOVA with Dunnett's multiple comparisons test based on mean values per experiment. *P* values are shown above plots.

to the periphery of the cytoplasm. Peripheral redistribution of organelles was also observed in ~20 to 50% of cells that had combined rapalog and arsenite treatment. Only the target organelle was dispersed following rapalog addition (fig. S16), confirming the specificity of the system.

The heterogeneity in response to rapalog in the arsenite-treated cell lines gave us the opportunity to compare the consequences of individual organelles being clustered or dispersed under internally controlled conditions. We therefore performed single-cell analysis (fig. S17A) to examine the relationship between spreading of each organelle and expression of genes whose induction by arsenite is sensitive to disruption of microtubules and dynein. In these experiments, we used immunostaining to monitor protein levels of heat shock protein family A member 6 (HSPA6), a molecular chaperone of the Hsp70 family (*52*, *53*), and heme oxygenase 1 (HMOX1), which degrades toxic heme produced by oxidative damage (*54*). While dispersion of lysosomes by KIF5B did not significantly affect HSPA6 induction by arsenite, this process was impaired by individually spreading mitochondria, recycling endosomes or the Golgi (Fig. 6A and fig. S17, B to E). Thus, robust activation of HSPA6 expression depends on the combinatorial action of multiple organelles in the perinuclear cytoplasm. In the case of HMOX1, forced dispersal of lysosomes, mitochondria, or recycling endosomes did not significantly alter expression output following arsenite treatment (Fig. 6B and fig. S18, A to D). In contrast, peripheral spreading of the Golgi reduced induction of this protein. Thus, maximal expression of HMOX1 in response to oxidative stress selectively requires clustering of the Golgi in the perinuclear region.

Collectively, these results demonstrate that disrupting perinuclear localization of membrane-bound organelles by dynein differentially affects stress-induced gene expression. Depending on the target gene, robust activation requires coordinated inputs from multiple organelles in the perinuclear region or the positioning of a single compartment at this site.

Last, we asked whether organelle clustering is sufficient to stimulate adaptive gene expression. This was achieved by replacing the KIF5B sequences in our organelle tethering system with those derived from the N-terminal region of the dynein-dynactin adaptor BICD2, which induces retrograde transport of associated organelles (*55*, *56*) (fig. S19A). Enforced perinuclear clustering of mitochondria, lysosomes, recycling endosomes, or the Golgi by tethering BICD2 sequences was not sufficient to trigger expression of HSPA6 or HMOX1 when arsenite was absent (fig. S19, B and C). These data reveal that perinuclear organelle clustering works in concert with other stress-induced processes to augment adaptive gene expression.

DISCUSSION

Summary

Cells cope with environmental insults by initiating a coordinated set of adaptive responses, including remodeling of the proteome through changes in transcription and translation. Stress also stimulates the formation of large membraneless compartments, including cytoplasmic stress granules and processing bodies, although the contribution these structures make to cellular adaptation is unclear (*7*). Here, we reveal another mesoscale change in cellular organization that occurs under stressed conditions: the enhanced perinuclear clustering of multiple membrane-bound organelles in response to oxidative insults. This evolutionarily conserved process, which we term SPOT, is orchestrated by PKC and the microtubule motor dynein, which drives retrograde transport of organelles in response to ROS. In this way, dynein translates oxidative stress into a pronounced reorganization of intracellular architecture. We show that targeting microtubules, dynein, or PKC reduces arsenite-induced expression of genes associated with proteostasis. We also demonstrate that acute dispersion of specific organelles from the perinuclear region diminishes induction of these genes, with individual compartments making distinct contributions to this process. Together, these findings support a model in which adaptive changes in gene expression in response to oxidative stress are enhanced through perinuclear clustering of multiple organelles by dynein (Fig. 7). However, organelle clustering at this site is not sufficient to stimulate adaptive gene expression in the absence of a stressor, indicating that this process collaborates with additional oxidative stress–induced signaling events that regulate transcription.

SPOT mechanism

The vast majority of studies of cytoskeletal transport have been conducted in cells grown under basal conditions. Thus, there is an incomplete picture of how cargo trafficking by motors responds to external stimuli. Our data reveal that PKC, which is activated by ROS via several redox-dependent processes (*57*), plays a key role in upregulating organelle trafficking by dynein in response to oxidative stress. While several kinases have previously been implicated in the regulation of dynein-based cargo transport—including extracellular signal–regulated kinase 1/2 (ERK1/2) (*58*), glycogen synthase kinase–3β (GSK-3β) (*59*), protein kinase A (PKA) (*60*), adenosine monophosphate–activated kinase (AMPK) (*61*), cyclin-dependent kinase 1 (CDK1), and Polo-like kinase 1 (PLK1) (*62*)—to our knowledge, PKC has not previously been reported to participate in this process.

We show that activation of PKC and SPOT by oxidative stress is not accompanied by global changes in dynein's association with dynactin or LIS1. This observation points to the involvement of a noncanonical mechanism for motor activation. PKC does, however, trigger rapid release of NDEL1 from dynein, identifying this event as a candidate driver of SPOT. NDEL1 is a phosphoprotein (*63*) that directly associates with the motor complex to enhance (*64*) or attenuate (*65*, *66*) its activity, depending on the context. In vitro reconstitution studies suggest that NDEL1 exerts opposing effects on dynein by priming the motor for transport via coupling to LIS1 (*64*, *67*–*69*), while simultaneously restraining its motility by limiting dynactin association (*65*, *70*). Although the release of NDEL1 is consistent with this protein acting as a negative regulator of dynein during SPOT, the unchanged association of the motor complex with LIS1 and dynactin during these events raises the possibility that NDEL1 exerts its inhibitory effect on preassembled dynein-dynactin complexes. If substantiated, then this would extend the involvement of NDEL1 in dynein's biology beyond its currently proposed role in early assembly processes and thereby add to growing evidence that regulation of this motor is more complex than previously appreciated (*71*, *72*). However, PKC might also stimulate retrograde transport through phosphoregulation of other components of the transport machinery, including the kinesin motor machinery that antagonizes dynein function on bidirectional cargoes.

The regulation of retrograde trafficking by PKC appears be achieved in concert with other signaling proteins, as our pharmacological inhibition experiments implicate several other kinases in relocalization of a subset of organelles following arsenite treatment (Fig. 3A). One conceivable route for cargo-specific regulation by kinases is phosphorylation of dynein's activating adaptors, a mechanism known to modulate organelle transport in some contexts (*62*, *73*). Collectively,

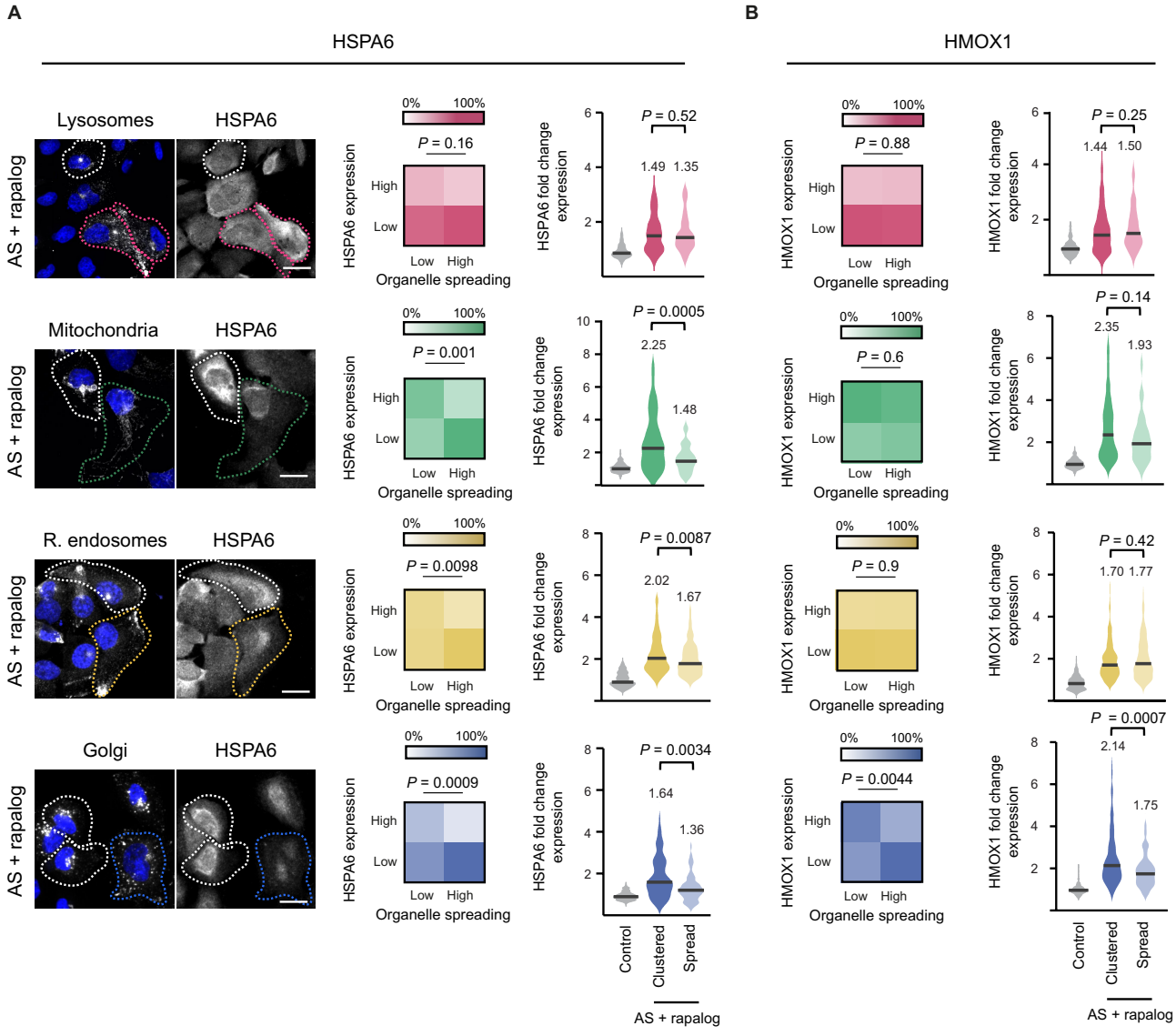

Fig. 6. Organelle repositioning has differential effects on gene expression. (**A**) Analysis of effect of KIF5B-mediated dispersal of indicated organelles on HSPA6 protein induction in arsenite-treated U2OS cells. Left: Representative confocal images of cells showing (in grayscale) organelle localization (HA) or HSPA6 protein in cells treated with 150 μM arsenite and 10 nM rapalog for 4 hours (30-min rapalog pretreatment followed by treatment with rapalog and arsenite). Dashed lines highlight cells with organelles that are clustered (white lines) or spread (colored lines). Scale bars, 30 μm. Heatmaps indicate percentage of cells in the categories of high and low HSPA6 expression (>2- or <2-fold change compared to untreated control cells) and high and low organelle spreading (>2- or <2-fold change compared to arsenite-treated cells in absence of rapalog). Charts show HSPA6 expression levels in control cells and in cells with clustered (<2-fold change in spreading) or spread (>2-fold change in spreading) organelles following arsenite and rapalog treatment. Violin plots show values for individual cells (>100 per condition), with the median value given and shown as a horizontal line. (**B**) Analysis of effect of organelle dispersal on HMOX1 induction in arsenite-treated U2OS cells. Data are plotted in heatmaps and violin plots as in (A). See fig. S18 for example images from HMOX1 experiments. Statistical significance was evaluated with a Fisher's exact test (for heatmaps) or a Mann-Whitney test (for violin plots). Data are aggregated from three independent experiments per protein analyzed. *P* values are shown above plots.

our observations are consistent with PKC promoting core dynein activity in response to ROS, with additional kinase pathways ensuring robust localization of specific cargoes. Deciphering the molecular details of transport regulation by PKC and other kinases will be an important goal of future work.

SPOT function

While we cannot rule out SPOT having additional functions in the adaptive response to oxidative stress, our data support a model in which this process enhances stress-induced transcription of genes that promote cellular adaptation, including proteostasis. It has been proposed that retrograde transport of mitochondria is a major driver of heat shock–induced activation of genes associated with protein quality control (*12*). These conclusions were based in large part on preventing mitochondrial clustering by disrupting microtubules or inhibiting dynein function. However, we have shown that these perturbations prevent perinuclear clustering of multiple organelles in stressed cells. By coupling a system for inducible dispersal of specific organelles to

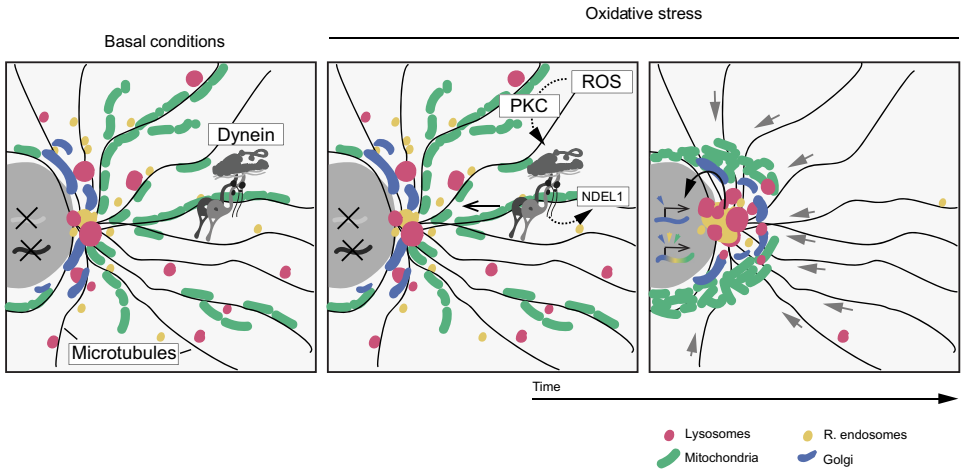

Fig. 7. Model for SPOT mechanism and function. Upon oxidative stress, increased ROS production activates PKC, which augments dynein-based retrograde transport of organelles. These events are accompanied by release of NDEL1 from dynein. Spatial reorganization of organelles differentially modulates adaptive gene expression in the nucleus. While transcription of some genes is stimulated by combinatorial inputs from multiple relocalized organelles (e.g., HSPA6), others (e.g., HMOX1) are regulated by a subset of these organelles (colored arrowheads).

single-cell readouts of gene expression, we have revealed that efficient induction of HSPA6 by oxidative stress depends not only on perinuclear localization of mitochondria but also on that of recycling endosomes and the Golgi. Moreover, we have found that perinuclear accumulation of the Golgi, but not other organelles, potentiates induction of HMOX1. Thus, coordinated positioning of multiple organelles contributes to the upregulation of genes in response to oxidative stress.

Dissecting the mechanisms by which localization of distinct organelles shapes the transcriptional response to oxidative stress will require further long-term investigation. Nonetheless, established paradigms for organelle-to-nucleus communication provide a useful framework for considering how these effects could arise. In principle, perinuclear clustering of multiple membrane-bound organelles could facilitate communication between these compartments, which could, in turn, influence the activation state or nuclear access of transcription factors that mediate stress-responsive changes in gene expression. This phenomenon has been proposed to contribute to retrograde signaling from mitochondria in response to stress, in which these organelles contact the nuclear envelope and thereby influence cholesterol-based regulation of nuclear factor κB (NFκB) activity in the nucleus (*74*). A requirement for interorganelle communication could explain why we observe contributions of mitochondria, Golgi, and recycling endosomes to HSPA6 induction. Given that these three compartments associate with signaling enzymes (*75*–*77*), it is also conceivable that concentration of these organelles in the perinuclear region enhances signaling toward transcription factor targets. These proteins could then regulate transcription of genes either in concert or independently, thereby linking organelle positioning to the selective gene expression outputs observed under stressed conditions. Alternatively, the strong enrichment of organelles in the perinuclear region following SPOT could cause local alterations in cytoskeletal tension that are mechanically transmitted to the nucleus to influence gene expression (*78*, *79*). The tools we have developed to acutely manipulate positioning of specific organelles pave the way for distinguishing between these and other hypothetical mechanisms for coupling spatial organization of the cytoplasm to remodeling of gene expression.

Outlook

By establishing a link between ROS, positioning of multiple organelles and transcriptional control, our findings raise the possibility that SPOT contributes to adaptive changes in gene expression in diseases that are associated with chronic or fluctuating oxidative stress, including atherosclerosis (*80*), cancer (*81*), type II diabetes (*82*), and inflammatory bowel disease (*83*). Exploring this notion may inform the development of diagnostic strategies or therapeutic opportunities. For example, antioxidant therapies for oxidative stress–associated pathologies have recently been shown to have substantial limitations, including interference with essential ROS signaling processes (*84*). Modulating perinuclear organelle transport may constitute a more selective strategy for influencing adaptive responses to oxidative stress in a therapeutic setting.

Beyond stress contexts, our work highlights a potential broader link between spatial positioning of membrane-bound organelles and gene expression regulation. Large-scale redistribution of organelles occurs in a variety of physiological settings in response to extrinsic cues. For example, migrating fibroblasts reorientate the Golgi along the front-rear axis of the cell in response to polarity signaling (*85*, *86*), and cells undergoing induced pluripotency transiently cluster their mitochondria in the perinuclear region (*87*). Each of these settings uses dynein for organelle repositioning, indicating that the molecular mechanisms responsible for these rearrangements could be shared with those driving SPOT.

MATERIALS AND METHODS

Antibodies and small molecules

Antibodies and small molecules used in this study are listed in tables S1 to S3.

Cell culture

Unless stated otherwise, U2OS Flp-In T-REX cells, unmodified HeLa cells, and RPE-1 cells were cultured at 37°C with 5% CO_2 in complete Dulbecco's modified Eagle's medium (DMEM) [high-glucose

DMEM + GlutaMAX (Gibco)], 10% fetal bovine serum (FBS; Gibco), and 1% (v/v) penicillin/streptomycin solution (Gibco). Flp-In T-REX cells were maintained in the presence of zeocin (100 μg/ml) and blasticidin (5 μg/ml; Gibco). The MycoAlert kit (Lonza) was used to check for the absence of *Mycoplasma* at the onset of the study. U2OS Flp-In T-REX cells expressing GFP were described previously (*88*). For glucose deprivation, minimal DMEM (no D-glucose, no L-glutamine, and no sodium pyruvate) (Gibco) supplemented with GlutaMAX (Gibco) was used. To confirm that effects of this medium on organelle localization were due to the absence of glucose, controls were performed with supplementation of D-glucose to a final concentration of 4.5 g/liter.

Mouse ES cell culture and spheroid generation

E14 (embryonic day 14) mouse ES cells (mESCs) were cultured as previously described (*17*, *89*) in gelatin-coated plates in Fc medium {DMEM (Thermo Fisher Scientific), 15% FBS, 1% (v/v) penicillin/streptomycin solution, GlutaMAX, sodium pyruvate (Thermo Fisher Scientific), minimum essential medium nonessential amino acids (Thermo Fisher Scientific), and 100 μM β-mercaptoethanol) supplemented with 2i/LIF [1 μM mitogen-activated protein kinase kinase inhibitor PD0325901 (Cambridge Stem Cell Institute), leukemia inhibitory factor (10 ng/ml; Cambridge Stem Cell Institute), and 3 μM GSK3 inhibitor CHIR99021 (Cambridge Stem Cell Institute)]}. To generate mESC spheroids, cells were dissociated and dissolved in N2B27 medium. In parallel, an eight-well ibiTreat Ibidi dish was coated with 540 μl of growth factor–reduced Matrigel, which was allowed to solidify at 37°C for 15 min. A total of 10,000 cells per well were plated on top of the Matrigel and incubated for 15 min at 37°C to allow attachment. The medium was subsequently replaced with cold N2B27 containing 5% dissolved Matrigel. Cells were cultured for 72 hours with a medium change performed at 24 to 48 or 48 to 72 hours to allow spheroid formation before fixation and processing for immunostaining. N2B27 contained a 1:1 mix of DMEM F12 (Thermo Fisher Scientific) and Neurobasal A (Thermo Fisher Scientific) supplemented with 1% (v/v) B27 (Thermo Fisher Scientific), 0.5% (v/v) N2 (homemade), 100 μM β-mercaptoethanol (Thermo Fisher Scientific), 1% (v/v) penicillin-streptomycin, and GlutaMAX (Thermo Fisher Scientific). N2 supplement contained DMEM F12 medium (Thermo Fisher Scientific), 0.75% bovine albumin fraction V (Thermo Fisher Scientific), insulin (2.5 mg/ml; Sigma-Aldrich), apotransferrin (10 mg/ml; Sigma-Aldrich), progesterone (2 μg/ml; Sigma-Aldrich), sodium selenite (0.6 μg/ml; Sigma-Aldrich), and putrescine dihydrochloride (1.6 mg/ml; Sigma-Aldrich).

Plasmids

Molecular cloning was performed using Gibson Assembly [Gibson Assembly Master Mix, New England Biolabs (NEB)]. For stable cell line generation, desired coding sequences were cloned in a pcDNA5-FRT/TO or pcDNA5-FRT/TO-eGFP backbone containing a tetracycline-inducible cytomegalovirus (CMV) promoter (*88*). pcDNA5-DYNC1I2-eGFP, pcDNA5-eGFP-BICD2N (N-terminal region of BICD2, 1 to 400 amino acids), and pcDNA5-eGFP-RAB6A were cloned with human open reading frames [UniProt IDs: DYNC1I2, Q13409 (isoform IC2C); BICD2, Q8TD16; RAB6A, P20340]. The following bicistronic plasmids using the self-cleaving P2A peptide were generated for the chemically induced heterodimerization system: pcDNA5-KIF5B-GFP-FKBP1A-P2A-FRB*-HA-MAOA^{tail}, pcDNA5-KIF5B-GFP-FKBP1A-P2A-FRB*-HA-GIANTIN^{tail}, pcDNA5-KIF5B-GFP-FKBP1A-P2A-FRB*-HA-RAB11A, pcDNA5-KIF5B-GFP-FKBP1A-P2A-LAMP1-HA-FRB*, pcDNA5-BICD2N-GFP-FKBP1A-P2A-FRB*-HA-MAOA^{tail}, pcDNA5-BICD2N-GFP-FKBP1A-P2A-FRB*-HA-GIANTIN^{tail}, pcDNA5-BICD2N-GFP-FKBP1A-P2A-FRB*-HA-RAB11A, and pcDNA5-BICD2N-GFP-FKBP1A-P2A-LAMP1-HA-FRB* [where FRB* is a variant of FRB that is targeted by rapalog but not rapamycin (*90*)]. These plasmids used sequences derived from the following UniProt IDs: KIF5B, P33176 (amino acids 1 to 413); BICD2, Q8TD16 (amino acids 1 to 594, BICD2N); FKBP1A, P62042; FRB domain of the mechanistic target of rapamycin kinase with the Thr^{2098} → Leu mutation, P42345 (amino acids 2021 to 2113); LAMP1, P11279; MAOA, P21397 (amino acids 481 to 527); and GIANTIN (GOLGB1), Q14789 (amino acids 3131 to 3259). The sequences of all plasmids were confirmed by Sanger or whole-plasmid sequencing.

Transfection and Flp-In T-REX cell line generation

U2OS Flp-In T-REX cells in six-well plates (1.5×10^5 cells per well) were transfected with 0.5 μg of the pcDNA5 FRT/TO–based plasmid together with 1.5 μg of pOG44, which encodes Flp recombinase. The plasmids were mixed with 200 μl of OptiMEM (Gibco) and 6 μl of FuGENE (Promega), followed by a 10-min incubation at room temperature and addition of the mix to cultured cells in a dropwise manner. The transfection medium was removed after 24 hours and replaced with fresh culture medium. After culturing for a further 24 hours to ensure plasmid expression, antibiotic selection was performed with medium containing hygromycin B (150 μg/ml) and blasticidin (5 μg/ml; both from Gibco). Selection continued until the appearance of single colonies. These colonies were trypsinized, and individual cells were pooled to generate cell lines.

siRNA transfection

ON-TARGETplus siRNA SMARTpools (Dharmacon) were resuspended in 1× siRNA buffer (Dharmacon) to a final concentration of 20 μM. The following pools were used: *DYNC1H1* (siDYNC1H1), L-00G828-00; *PAFAH1B1/LIS1* (siLIS1), L-010330-00; *PRKCA*, L-003523-00; *PRKCD*, L-003524-00; *PRKCE*, L-004653-00; *PRKCH*, L-004655-00; *PRKCQ*, L-003525-00 and nontargeting (siControl), D-001810-10 (see table S4 for siRNA sequences). Cell transfections were performed in 24- or 6-well plates. For the 24-well format, 0.02 μmol of siRNA was incubated with 1.5 μl of Lipofectamine RNAiMAX (Invitrogen) in 50 μl of OptiMEM (Gibco) for 10 min at room temperature, followed by mixing with 450 μl of culture medium and 8×10^4 trypsinized cells per well. For six-well plates, 0.1 μmol of siRNA, 7.5 μl of Lipofectamine RNAiMAX, and 250 μl of OptiMEM was used, together with 1.5 ml of culture medium and 1.92×10^5 trypsinized cells per well. In both formats, transfection medium was replaced with fresh culture medium 24 hours later, with cells cultured for a further 48 hours before fixation and processing for immunostaining or RNA extraction.

Drosophila culture, strains, and egg chamber treatment

The *Drosophila melanogaster* yellow fluorescent protein (YFP)–Rab11 strain [which has a knock-in of YFP into the endogenous gene (*91*)] was cultured with food containing 5.5% (w/v) glucose, 3.5% (w/v) organic wheat flour, 0.75% (w/v) agar, 5% (w/v) baker's yeast, 0.004% propionic acid, and 16.4 mM methyl-4-hydroxybenzoate. Cultures were maintained in an environmentally controlled fly room set to 25°C and 50% relative humidity with a repeating 12-hour light/12-hour dark regime. Egg chambers were dissected from mated females in Schneider's

medium (Gibco). Following one wash in Schneider's medium, the chambers were incubated in Schneider's medium ± 300 μM sodium arsenite (Merck) for 1 hour at room temperature before fixation and immunostaining, as described below. Quantification was performed on stage 13 to 14 egg chambers.

Immunoprecipitation

To induce the expression of GFP, DYNC1I2-GFP, or GFP-BICD2N, U2OS cell lines were cultured in the presence of tetracycline (1 μg/ml) for 48 hours in 15-cm dishes. Cells were harvested, washed in phosphate-buffered saline (PBS), and lysed in 200 μl of iced-cold lysis buffer [10 mM tris-HCl (pH 7.4), 150 mM NaCl, 0.5 mM EDTA, 5% NP-40, 1 mM phenylmethylsulfonyl fluoride containing protease (cOmplete EDTA-free, Sigma-Aldrich), and phosphatase (PhosSTOP EASYpack, Sigma-Aldrich) inhibitors] for 30 min. Lysates were then centrifuged at 16,000*g* for 15 min, and the supernatant was transferred to precooled 1.5-ml Eppendorf tubes and diluted 1:1 in detergent-free lysis buffer. Protein concentration was measured with Bradford reagent (Thermo Fisher Scientific) and equalized across samples. Twenty microliters of equilibrated GFP-Trap_MA bead slurry (Chromotek) was added to each diluted supernatant, followed by end-over-end tumbling for 1 hour at 4°C. Using a magnetic rack, beads were washed three times in wash buffer [5 mM tris-HCl (pH 7.4), 80 mM NaCl, and 1% Triton X-100]. For analysis by immunoblotting, immunoprecipitates were eluted and boiled (95°C for 5 min) in 2× Laemmli sample buffer [120 mM tris-HCl (pH 6.8), 4% SDS, 20% glycerol, 10% β-mercaptoethanol, and 0.02% bromophenol blue] for subsequent analysis. For mass spectrometry analysis, beads were washed twice in wash buffer and twice in Triton X-100–free wash buffer, dried, and frozen for subsequent mass spectrometry analysis.

Immunoblotting

Samples for immunoblotting were prepared with 2× Laemmli sample buffer to a final 1× concentration and then resolved by SDS–polyacrylamide gel electrophoresis (PAGE) using 4 to 12% NuPAGE bis-tris gels (Thermo Fisher Scientific). Proteins were then wet transferred to methanol-activated Immobilon PVDF membrane (Millipore). Blocking was performed in 5% (w/v) skimmed milk (Marvel) in PBS for 15 min at room temperature. Primary antibodies were incubated with the membrane overnight at 4°C (see table S1 for details of antibodies and their working dilutions). After washing in PBS, membranes were incubated with horseradish peroxidase–conjugated secondary antibodies (diluted 1:10,000 in PBS; table S2) for 1 hour at room temperature. Signals were developed using the ECL Prime system (Cytiva) and Super RX-N medical x-ray film (FUJIFILM).

Mass spectrometry analysis

Beads were resuspended in Hepes buffer [20 mM Hepes (pH 8.0) and 3 mM $MgCl_2$] containing 0.1% RapiGest (Waters). Protein was reduced using 5 mM dithiothreitol (DTT) at 56°C for 30 min, followed by alkylation with 10 mM iodoacetamide at room temperature for 30 min. One microgram of trypsin (Promega) was added to the bead suspension and incubated for 8 hours at 37°C. TMTpro 18plex reagent (250 μg; Thermo Fisher Scientific) was added to each sample, followed by incubation at room temperature for 1 hour. The labeling reaction was stopped by incubation with 9 μl of 5% hydroxylamine for 30 min. Labeled peptides were combined into a single TMT multiplex, dried to completion, and desalted using Peptide Desalting spin columns (Thermo Fisher Scientific). The peptides were then analyzed by liquid chromatography–tandem mass spectrometry (LC-MS/MS) using the Thermo Vanquish Neo Nano System, fitted with a PepMap Neo C18, 5-μm 0.3 mm–by–5 mm nano trap column (Thermo Fisher Scientific) and an Aurora Ultimate TS 75 μm–by–25 cm–by–1.7 μm C18 column (IonOpticks). Peptides were separated using buffer A (0.1% formic acid) and buffer B (80% acetonitrile and 0.1% formic acid) at a column temperature of 40°C and a flow rate of 300 nl/min. Eluted peptides were introduced directly via a nanoFlex ion source into an Orbitrap Eclipse mass spectrometer equipped with FAIMS (Thermo Fisher Scientific). To increase depth, each sample was acquired with three different FAIMS compensation voltages. The mass spectrometer was operated in real-time database search (RTS) with synchronous-precursor selection–MS3 analysis for quantification of reporter ions. MS1 spectra were acquired using the following settings: resolution, 120 K; mass range, 400 to 1400 mass/charge ratio (m/z); AGC target, 4×10^5; MaxIT, 50 ms; and dynamic exclusion, 60 s. MS2 analysis were carried out with HCD activation and ion trap detection with the following settings: AGC, 10^4; MaxIT, 50 ms; NCE, 33%; and isolation window, 0.7 m/z. RTS of MS2 spectra was set up to search UP000005640_9606 *Homo sapiens* proteome (20,582 protein sequences), with fixed modifications cysteine carbamidomethylation and TMTpro 16plex at N-terminal and lysine residues. Methionine-oxidation was set as a variable modification. Missed cleavage was set at 1, and maximum variable modification was set at 2. MS3 scans were performed with the close-out function enabled and the maximum number of peptides per protein set to 5. The selected precursors were fragmented by HCD and analyzed using the orbitrap with the following settings: isolation window, 0.7 m/z; NCE, 55; orbitrap resolution, 120 K; scan range, 110 to 450 m/z; MaxIT, 300 ms; and AGC, 1.5×10^5. The raw LC-MS/MS data were processed with Sequest HT in Proteome Discoverer (v.3.1). MS/MS spectra for TMTpro 18plex experiments were quantified using reporter ion MS3 and searched against the UP000005640_9606 *H. sapiens* proteome. Carbamidomethylation of cysteines was specified as a fixed modification, with methionine oxidation and N-terminal acetylation (protein) set as variable modifications.

Scaled abundances were calculated using Proteome Discoverer, representing protein quantification values normalized across TMT channels to account for differences in sample loading and instrument response. This enabled direct comparison between samples. These scaled abundances were then used for downstream analysis. For each replicate, protein abundances were $\log_2$ transformed and normalized to the amount of GFP-tagged bait protein to correct for differences in immunoprecipitation efficiency. Mean $\log_2$-scaled abundances across replicates were subsequently calculated and used for plotting and for linear regression analysis comparing control and arsenite-treated samples.

Cell staining and imaging

For immunostaining of adherent human cells (U2OS, HeLa, and RPE-1), cells were cultured on coverslips in 24-well plates. mESC-derived spheroids were grown in Matrigel, as described above. Cells and spheroids were fixed in PBS containing 4% paraformaldehyde for 10 min at 37°C, washed twice in PBS, and permeabilized in 0.1% Triton X-100 at 4°C for 5 min. After washing, cells were blocked for 20 min in PBS containing 2% bovine serum albumin (BSA; Merck). Primary antibodies were prepared in antibody solution (0.1% BSA in PBS) and incubated with samples for 1 hour at room temperature (see table S1 for details and working dilutions). Samples were then washed in antibody solution and incubated with Alexa Fluor–labeled

secondary antibodies prepared in antibody solution (see table S2 for details and working dilutions). 4′,6-Diamidino-2-phenylindole (DAPI; 1:1000 dilution; Thermo Fisher Scientific) (to label the nucleus) or Alexa Fluor 555–wheat germ agglutinin (WGA; 1:100 dilution; Thermo Fisher Scientific) (to determine cell area) were incubated together with the secondary antibodies. Last, cells were washed in PBS and mounted on slides using Prolong Gold Antifade Mountant (Invitrogen). Imaging was performed with a Zeiss 780 laser scanning confocal microscope using 40×/1.4 numerical aperture (NA) or 63×/1.3 NA oil immersion objectives.

For live imaging, U2OS cells were plated in eight-well glass-bottomed μ-Slides (ibidi). For labeling of lysosomes, mitochondria, or recycling endosomes, cells were treated, respectively, with LysoTracker (Thermo Fisher Scientific), MitoTracker Deep Red FM (Thermo Fisher Scientific), or Alexa Fluor 647–human transferrin (Thermo Fisher Scientific; 30-min pretreatment to allow trafficking of transferrin to the recycling endosome compartment). For trans-Golgi network (TGN) imaging, the pcDNA5-eGFP-RAB6A plasmid was transfected 24 hours before imaging. Basal expression of the insert from the CMV promoter in the absence of tetracycline generated sufficient signal for visualization. Images were captured during a 1-hour treatment with 300 μM arsenite treatment at 2 frames/min using a Nikon W1 spinning disk confocal equipped with a 60×/1.4 NA water immersion objective.

Drosophila egg chambers were fixed in 4% paraformaldehyde for 20 min. Permeabilization was performed in PBS/1% Triton X-100 for 1 hour at room temperature, followed by blocking in PBS/0.1% Tween 20 (PBST) containing 10% BSA. Primary and secondary antibodies (tables S1 and S2) were prepared in PBST containing 0.1% BSA and incubated with egg chambers overnight at 4°C or for 2 hours at room temperature, respectively, with washes performed in PBST. At the end of the procedure, samples were mounted in VECTASHIELD containing DAPI (Vector Laboratories) and imaged with a Zeiss 780 laser scanning confocal microscope using a 40×/1.4 NA oil immersion objective.

Image analysis

Images were analyzed using a custom Python pipeline integrated with Fiji/ImageJ (*92*). Briefly, whole cells were segmented on the basis of WGA signal to define regions of interest (ROIs), within which objects were segmented from a separate channel. The area of each cell was calculated directly from the segmented ROI. To quantify the spatial distribution of objects within each cell, a signed distance map was computed for each ROI. Object spread was defined as the intensity-weighted spatial dispersion of object pixels within the ROI, calculated as the square root of the summed variances of object pixel coordinates relative to their intensity-weighted centroid. Mean intensity of the selected channel was computed as the average pixel intensity within the segmented cell ROI. All measurements were exported into GraphPad Prism (version 10) or Microsoft Excel for compilation and statistical analysis (see below).

Line scan analysis was performed using Fiji/ImageJ. A straight line was drawn across the region of interest in a multichannel image. The intensity profile along this line (plot profile) for each channel (lysosomes, mitochondria, and TGN) was generated as a function of distance along the line. The resulting intensity values were exported for further analysis and visualization.

For analysis of organelle distribution in mESC-derived spheroids, cell shape was determined by WGA staining. Distance between the nucleus and the recycling endosome compartment per cell was calculated from the edge of the nucleus to the RAB11A-positive compartment. To quantify distribution of mitochondria, equivalently sized ROIs were drawn in the basal (outer half of the cell) and apical (half of the cell facing the lumen of the spheroid) regions of individual cells, followed by determination of fluorescent intensities in these regions in Fiji/ImageJ. To calculate Golgi localization, total spheroid area and area covered by the Golgi were calculated on the basis of WGA and GM130 staining, respectively, and the values were expressed in terms of radial distance from the lumen.

Drosophila egg chambers were manually classified according to the spatial distribution of recycling endosomes, mitochondria, and Golgi signals. On the basis of these patterns, each egg chamber was assigned to one of three phenotypic categories: clustered, intermediate, or spread.

Pericentrosomal enrichment of DCTN1 and KIF5B was quantified by measuring fluorescence intensities as follows. A circular ROI of 4.5 μm^2 was manually placed over the pericentrosomal area, identified on the basis of centrosome-associated signal in the corresponding channel. Mean fluorescence intensity within this ROI was measured and compared to the mean cytosolic intensity obtained from a larger ROI positioned within the cytoplasm of the same cell that did not include the pericentrosomal region. Pericentrosomal enrichment was calculated as the ratio of the pericentrosomal mean intensity to the cytosolic mean intensity for each cell.

Immunoblot band intensities were quantified by densitometry using the Fiji/ImageJ built-in Gel Analysis workflow. Briefly, rectangular regions corresponding to each lane were defined and intensity profiles along the migration axis of the blot generated. Signal associated with each band was quantified by integrating the area under the corresponding peak of intensity after defining a baseline. The resulting band intensities were then normalized to signals for α-tubulin (for cell lysates) or the corresponding bait (for immunoprecipitates).

Ubiquitination assay

Twenty-four hours before the experiment, cells were plated in 24-well plates (1.2×10^5 cells per well). After treatments (see fig. S15), cells were lysed in 10 mM tris-HCl (pH 7.4), 150 mM NaCl, 0.5 mM EDTA, and 1% Triton X-100, containing protease inhibitor (cOmplete EDTA-free) and benzonase (Merck). Protein concentration was measured with Bradford reagent (Thermo Fisher Scientific) and equalized across samples. Ubiquitinated proteins were resolved by SDS-PAGE using 4 to 12% NuPAGE bis-tris gels, as described above. Immunoblotting was performed as previously described using an anti–ubiquitin antibody (table S1). Signals were quantified using ImageJ, and the protein ubiquitination signal was normalized to the levels of α-tubulin in the corresponding loading control.

Crystal violet assay

For experiments assessing cell survival in response to stress, cells were plated in 96-well plates (1.5×10^4 cells per well) 24 hours before treatments. After the experiment, cells were fixed in methanol at −20°C for 10 min and stained with crystal violet solution (1%, w/v; Sigma-Aldrich) for 10 min at room temperature. The absorbance at 592 nm per well was then measured with a PHERAstar FSX microplate reader (BMG Labtech).

Reverse transcription-quantitative polymerase chain reaction

Before the experiment, cells were plated in six-well plates (1.92×10^5 cells per well). Following washing in ice-cold PBS, cells were lysed in 40 mM DTT RLT buffer [provided in the RNeasy extraction kit (QIAGEN)]. Total RNA was then extracted following the RNeasy extraction kit protocol. Subsequently, 500 ng of total RNA were reverse transcribed using the Applied Biosystems High-Capacity RNA-to-cDNA kit (Thermo Fisher Scientific). Ten nanograms of cDNA was analyzed per sample using SYBR Green Universal Master Mix (Thermo Fisher Scientific) and gene-specific primers (see table S5). Relative expression was calculated by normalization to *glyceraldehyde-3-phosphate dehydrogenase* (*GAPDH*) and *hypoxanthine-guanine phosphoribosyltransferase* (*HPRT*) genes.

RNA sequencing

Library preparation

Total RNA was extracted as described above and its concentration determined with the Qubit RNA BR assay kit (Invitrogen). Sufficient RNA quality (RIN > 9) was confirmed using a Bioanalyzer and RNA 6000 Pico Kit (Agilent). One microgram of total RNA per sample was used for mRNA isolation with the NEBNext poly(A) mRNA magnetic isolation module (NEB). Libraries were generated using the NEBNext Ultra II directional RNA library prep kit for Illumina (NEB) following the manufacturer's instructions. Libraries were then barcoded with Multiplex Oligos for Illumina (Dual index primers pairs set 4, NEB). Library concentrations were determined with the Qubit dsDNA High Sensitivity (Invitrogen). Library quality and average size were assessed with a High Sensitivity DNA kit (Agilent). Pooled libraries (780 pM) were sequenced using the NextSeq 2000 system (NextSeq 2000 P3 100 cycles, Illumina) in paired-end 100 mode at a depth of 25 million reads per library.

RNA-seq data processing

Quality control, trimming, and mapping of FASTQ files was performed with the rnaseq pipeline (version 3.12.0) distributed by nf-core (https://zenodo.org/records/7998767). The pipeline was configured so that each component was version controlled and executed within a Singularity container (https://sylabs.io). The pipeline was executed with the following command: nextflow run nf-core/rnaseq -r 3.12.0 --input samplesheet.csv --genome homo_sapiens.GRCh38.release_102 -config lmb.config --outdir results --deseq2_vst -bg.

These parameters generally adhere to the defaults set by the nf-core rnaseq pipeline and use STAR (version 2.7.9a) as the aligner, with reads mapped to the human reference genome (GRCh38/release 102). The read trimming parameter --nextseq 20 was used to account for the Illumina color chemistry in which high-quality calls for guanine nucleotides can reflect no signal on a flow cell. The pipeline was also passed a sample list that detailed the forward and reverse FASTQ file pairings, along with sample identities and how replicates should be grouped together. The nf-core rnaseq pipeline yields quantitated expression values for each gene in each sample, reporting raw counts and transcripts per million values. These expression matrices were used in downstream analyses. Differential gene expression analysis was performed using the DESeq2 statistical framework as implemented in SeqMonk (version 1.48.1), using raw read counts per gene as input. Genes with a shrunk $\log_2$ fold change of >0.58 (i.e., >1.5-fold change) and an adjusted FDR of less than 0.05 were designated as differentially expressed.

Kinesin-1–mediated organelle dispersion

Flp-In T-REX U2OS stable cell lines expressing pcDNA5-KIF5B-GFP-FKBP1A-P2A-FRB*-HA-MAOA^{tail}, pcDNA5-KIF5B-GFP-FKBP1A-P2A-FRB*-HA-GIANTIN^{tail}, pcDNA5-KIF5B-GFP-FKBP1A-P2A-FRB*-HA-RAB11A, or pcDNA5-KIF5B-GFP-FKBP1A-P2A-LAMP1-HA-FRB* were generated as described above. An additional fluorescence-activated cell sorting step based on GFP expression in tetracycline-treated cells was performed to enrich for cells with high expression of the construct (upper quartile of the population).

For experiments assessing stress-responsive protein induction, cells were plated 48 hours beforehand in medium containing tetracycline (1 μg/ml) to induce transgene expression. Medium containing 10 nM rapalog (A/C heterodimerizer, Takara Bio) was added to the medium 30 min before replacement with medium containing 10 nM rapalog and 150 μM arsenite, followed by incubation for a further 4 hours. Control experiments were performed with no rapalog ± arsenite. Cells were fixed and stained as described above, with Alexa Fluor 555–WGA used to determine cell area, anti–hemagglutinin (HA) used to assess spreading of the organelle of interest, and antibodies against HSPA6 or HMOX1 used to measure induction of stress-responsive proteins. After imaging, single-cell analysis was performed using a custom analysis pipeline (see the "Image analysis" section). For each cell, organelle spreading and gene expression levels were quantified. A twofold threshold was used to classify cells according to both gene expression and organelle spreading: high (>2-fold) or low (<2-fold). For gene expression, the reference condition was untreated control cells (no rapalog and no arsenite). The organelle spreading cutoff was determined relative to arsenite-treated cells (no rapalog + arsenite). These thresholds were subsequently applied to the arsenite + rapalog condition. Association of variables was assessed using Fisher's exact test. Further, the magnitude of gene expression changes was calculated separately for cells exhibiting >2-fold organelle spreading ("spread") and <2-fold organelle spreading ("clustered").

BICD2-mediated organelle clustering

To assess the effect of organelle clustering in the absence of stress, the pcDNA5 constructs used for organelle dispersion were modified by substituting the motor domain of KIF5B with the N-terminal region of the dynein adaptor BICD2 (amino acids 1 to 594) (pcDNA5-BICD2N-GFP-FKBP1A-P2A-FRB*-HA-MAOA^{tail}, pcDNA5-BICD2N-GFP-FKBP1A-P2A-FRB*-HA-GIANTIN^{tail}, pcDNA5-BICD2N-GFP-FKBP1A-P2A-FRB*-HA-RAB11A, and pcDNA5-BICD2N-GFP-FKBP1A-P2A-LAMP1-HA-FRB*).

Flp-In T-REX U2OS cells were transfected in 24-well plates (8×10^4 cells per well) with 0.4 μg of the pcDNA5 plasmid. The plasmid was mixed with 200 μl of OptiMEM (Gibco) and 1.2 μl of FuGENE (Promega), followed by a 10-min incubation at room temperature and addition of the mix to cultured cells in a dropwise manner. The transfection medium was removed after 24 hours and replaced with fresh culture medium containing tetracycline (1 μg/ml) to induce expression of the construct. For experiments assessing the effect of organelle clustering, following 24 hours of incubation with tetracycline, cells were treated with 10 nM rapalog ±150 μM arsenite for 4 hours. Control experiments were performed with cells that were not exposed to the transfection mix but otherwise treated as above. Cells were fixed and stained to follow GFP (demonstrating successful transfection), organelle distribution, and stress-responsive proteins.

Following image acquisition, single-cell analysis was performed in ImageJ/Fiji to quantify the mean fluorescence intensity of the protein of interest (HSPA6 or HMOX1).

Statistical analysis

Data analyses and graphical representations were generated using GraphPad Prism (version 10) or Microsoft Excel (version 16.106.3). Statistical methods were selected on the basis of the verified or assumed distribution of the data (normal versus non-normal), variance homogeneity, sample size, and whether comparisons were conducted between two groups or multiple groups. Information about sample numbers and specific statistical tests applied is provided in the figures or figure legends.

Supplementary Materials

The PDF file includes:

Figs. S1 to S19
Tables S1 to S5
Legends for movies S1 to S4
Legends for datasets S1 and S2

Other Supplementary Material for this manuscript includes the following:

Movies S1 to S4
Datasets S1 and S2

REFERENCES

1. E. de Nadal, G. Ammerer, F. Posas, Controlling gene expression in response to stress. *Nat. Rev. Genet.* **12**, 833–845 (2011).
2. S. Fulda, A. M. Gorman, O. Hori, A. Samali, Cellular stress responses: Cell survival and cell death. *Int. J. Cell Biol.* **2010**, 214074 (2010).
3. S. Alberti, A. A. Hyman, Biomolecular condensates at the nexus of cellular stress, protein aggregation disease and ageing. *Nat. Rev. Mol. Cell Biol.* **22**, 196–213 (2021).
4. S. F. Banani, H. O. Lee, A. A. Hyman, M. K. Rosen, Biomolecular condensates: Organizers of cellular biochemistry. *Nat. Rev. Mol. Cell Biol.* **18**, 285–298 (2017).
5. Y. Li, Y. Liu, X.-Y. Yu, Y. Xu, X. Pan, Y. Sun, Y. Wang, Y.-H. Song, Z. Shen, Membraneless organelles in health and disease: Exploring the molecular basis, physiological roles and pathological implications. *Signal Transduct. Target. Ther.* **9**, 305 (2024).
6. A. Peng, S. C. Weber, Evidence for and against liquid-liquid phase separation in the nucleus. *Noncoding RNA* **5**, 5040050 (2019).
7. D. Mateju, J. A. Chao, Stress granules: Regulators or by-products? *FEBS J.* **289**, 363–373 (2022).
8. R. Parker, U. Sheth, P bodies and the control of mRNA translation and degradation. *Mol. Cell* **25**, 635–646 (2007).
9. R. Char, Z. Liu, C. Jacqueline, M. Davieau, M. G. Delgado, C. Soufflet, M. Fallet, L. Chasson, R. Chapuy, V. Camosseto, E. Strock, R. Rua, C. R. Almeida, B. Su, A. M. Lennon-Dumenil, B. Nal, A. Roquilly, Y. Liang, S. Meresse, E. Gatti, P. Pierre, RUFY3 regulates endolysosomes perinuclear positioning, antigen presentation and migration in activated phagocytes. *Nat. Commun.* **14**, 4290 (2023).
10. N. Rocha, C. Kuijl, R. van der Kant, L. Janssen, D. Houben, H. Janssen, W. Zwart, J. Neefjes, Cholesterol sensor ORP1L contacts the ER protein VAP to control Rab7-RILP-p150 Glued and late endosome positioning. *J. Cell Biol.* **185**, 1209–1225 (2009).
11. L. T. Trinh, A. Van Vu, S. Shin, C. Lee, S. H. Park, E.-B. Cho, Y. Heo, H. J. Kim, S. Kim, J.-B. Yoon, RNF13 mediates pH- and Ca^{2+}-dependent regulation of lysosomal positioning. *Cell Rep.* **44**, 116053 (2025).
12. S. Agarwal, S. Ganesh, Perinuclear mitochondrial clustering, increased ROS levels, and HIF1 are required for the activation of HSF1 by heat stress. *J. Cell Sci.* **133**, 245589 (2020).
13. A.-B. Al-Mehdi, V. M. Pastukh, B. M. Swiger, D. J. Reed, M. R. Patel, G. C. Bardwell, V. V. Pastukh, M. F. Alexeyev, M. N. Gillespie, Perinuclear mitochondrial clustering creates an oxidant-rich nuclear domain required for hypoxia-induced transcription. *Sci. Signal.* **5**, ra47 (2012).
14. M. M. Emara, K. Fujimura, D. Sciaranghella, V. Ivanova, P. Ivanov, P. Anderson, Hydrogen peroxide induces stress granule formation independent of eIF2α phosphorylation. *Biochem. Biophys. Res. Commun.* **423**, 763–769 (2012).
15. R. V. Blackburn, D. R. Spitz, X. Liu, S. S. Galoforo, J. E. Sim, L. A. Ridnour, J. C. Chen, B. H. Davis, P. M. Corry, Y. J. Lee, Metabolic oxidative stress activates signal transduction and gene expression during glucose deprivation in human tumor cells. *Free Radic. Biol. Med.* **26**, 419–430 (1999).
16. S. M. Hong, C. W. Park, S. W. Kim, Y. J. Nam, J. H. Yu, J. H. Shin, C. H. Yun, S.-H. Im, K.-T. Kim, Y. C. Sung, K. Y. Choi, NAMPT suppresses glucose deprivation-induced oxidative stress by increasing NADPH levels in breast cancer. *Oncogene* **35**, 3544–3554 (2016).
17. M. N. Shahbazi, A. Scialdone, N. Skorupska, A. Weberling, G. Recher, M. Zhu, A. Jedrusik, L. G. Devito, L. Noli, I. C. Macaulay, C. Buecker, Y. Khalaf, D. Ilic, T. Voet, J. C. Marioni, M. Zernicka-Goetz, Pluripotent state transitions coordinate morphogenesis in mouse and human embryos. *Nature* **552**, 239–243 (2017).
18. M. A. Titus, Myosin-driven intracellular transport. *Cold Spring Harb. Perspect. Biol.* **10**, a021972 (2018).
19. N. Hirokawa, Y. Noda, Y. Tanaka, S. Niwa, Kinesin superfamily motor proteins and intracellular transport. *Nat. Rev. Mol. Cell Biol.* **10**, 682–696 (2009).
20. S. L. Reck-Peterson, W. B. Redwine, R. D. Vale, A. P. Carter, The cytoplasmic dynein transport machinery and its many cargoes. *Nat. Rev. Mol. Cell Biol.* **19**, 382–398 (2018).
21. W. O. Hancock, Bidirectional cargo transport: Moving beyond tug of war. *Nat. Rev. Mol. Cell Biol.* **15**, 615–628 (2014).
22. J. Lüders, T. Stearns, Microtubule-organizing centres: A re-evaluation. *Nat. Rev. Mol. Cell Biol.* **8**, 161–167 (2007).
23. S. R. Gill, T. A. Schroer, I. Szilak, E. R. Steuer, M. P. Sheetz, D. W. Cleveland, Dynactin, a conserved, ubiquitously expressed component of an activator of vesicle motility mediated by cytoplasmic dynein. *J. Cell Biol.* **115**, 1639–1650 (1991).
24. C. M. Waterman-Storer, S. B. Karki, S. A. Kuznetsov, J. S. Tabb, D. G. Weiss, G. M. Langford, E. L. Holzbaur, The interaction between cytoplasmic dynein and dynactin is required for fast axonal transport. *Proc. Natl. Acad. Sci. U.S.A.* **94**, 12180–12185 (1997).
25. K. Zhang, H. E. Foster, A. Rondelet, S. E. Lacey, N. Bahi-Buisson, A. W. Bird, A. P. Carter, Cryo-EM reveals how human cytoplasmic dynein is auto-inhibited and activated. *Cell* **169**, 1303–1314 (2017).
26. R. J. McKenney, W. Huynh, M. E. Tanenbaum, G. Bhabha, R. D. Vale, Activation of cytoplasmic dynein motility by dynactin-cargo adapter complexes. *Science* **345**, 337–341 (2014).
27. M. A. Schlager, H. T. Hoang, L. Urnavicius, S. L. Bullock, A. P. Carter, In vitro reconstitution of a highly processive recombinant human dynein complex. *EMBO J.* **33**, 1855–1868 (2014).
28. K. Singh, C. K. Lau, G. Manigrasso, J. B. Gama, R. Gassmann, A. P. Carter, Molecular mechanism of dynein-dynactin complex assembly by LIS1. *Science* **383**, eadk8544 (2024).
29. D. Splinter, D. S. Razafsky, M. A. Schlager, A. Serra-Marques, I. Grigoriev, J. Demmers, N. Keijzer, K. Jiang, I. Poser, A. A. Hyman, C. C. Hoogenraad, S. J. King, A. Akhmanova, BICD2, dynactin, and LIS1 cooperate in regulating dynein recruitment to cellular structures. *Mol. Biol. Cell* **23**, 4226–4241 (2012).
30. P. S. Brookes, Y. Yoon, J. L. Robotham, M. W. Anders, S. S. Sheu, Calcium, ATP, and ROS: A mitochondrial love-hate triangle. *Am. J. Physiol. Cell Physiol.* **287**, C817–C833 (2004).
31. V. Eisner, M. Picard, G. Hajnoczky, Mitochondrial dynamics in adaptive and maladaptive cellular stress responses. *Nat. Cell Biol.* **20**, 755–765 (2018).
32. M. T. Lin, M. F. Beal, Mitochondrial dysfunction and oxidative stress in neurodegenerative diseases. *Nature* **443**, 787–795 (2006).
33. W. Xiao, R. S. Wang, D. E. Handy, J. Loscalzo, NAD(H) and NADP(H) redox couples and cellular energy metabolism. *Antioxid. Redox Signal.* **28**, 251–272 (2018).
34. D. Averill-Bates, Reactive oxygen species and cell signaling. Review. *Biochim. Biophys. Acta Mol. Cell Res.* **1871**, 119573 (2024).
35. H. Sies, D. P. Jones, Reactive oxygen species (ROS) as pleiotropic physiological signalling agents. *Nat. Rev. Mol. Cell Biol.* **21**, 363–383 (2020).
36. M. Castagna, Y. Takai, K. Kaibuchi, K. Sano, U. Kikkawa, Y. Nishizuka, Direct activation of calcium-activated, phospholipid-dependent protein kinase by tumor-promoting phorbol esters. *J. Biol. Chem.* **257**, 7847–7851 (1982).
37. R. A. Butow, N. G. Avadhani, Mitochondrial signaling: The retrograde response. *Mol. Cell* **14**, 1–15 (2004).
38. M. Miaczynska, S. Christoforidis, A. Giner, A. Shevchenko, S. Uttenweiler-Joseph, B. Habermann, M. Wilm, R. G. Parton, M. Zerial, APPL proteins link Rab5 to nuclear signal transduction via an endosomal compartment. *Cell* **116**, 445–456 (2004).
39. P. M. Quiros, A. Mottis, J. Auwerx, Mitonuclear communication in homeostasis and stress. *Nat. Rev. Mol. Cell Biol.* **17**, 213–226 (2016).
40. A. Roczniak-Ferguson, C. S. Petit, F. Froehlich, S. Qian, J. Ky, B. Angarola, T. C. Walther, S. M. Ferguson, The transcription factor TFEB links mTORC1 signaling to transcriptional control of lysosome homeostasis. *Sci. Signal.* **5**, ra42 (2012).
41. E. M. Walker, G. L. Pearson, N. Lawlor, A. M. Stendahl, A. Lietzke, V. Sidarala, J. Zhu, T. Stromer, E. C. Reck, J. Li, E. Levi-D'Ancona, M. B. Pasmooij, D. L. Hubers, A. Renberg, K. Mohamed, V. S. Parekh, I. X. Zhang, B. Thompson, D. Zhang, S. A. Ware, L. Haataja, N. Qi, S. C. J. Parker, P. Arvan, L. Yin, B. A. Kaufman, L. S. Satin, L. Sussel, M. L. Stitzel, S. A. Soleimanpour, Retrograde mitochondrial signaling governs the identity and maturity of metabolic tissues. *Science* **388**, eadf2034 (2025).
42. Q. Ma, Transcriptional responses to oxidative stress: Pathological and toxicological implications. *Pharmacol. Ther.* **125**, 376–393 (2010).

43. F. Zhang, Y. Xiao, Y. Wang, SILAC-based quantitative proteomic analysis unveils arsenite-induced perturbation of multiple pathways in human skin fibroblast cells. *Chem. Res. Toxicol.* **30**, 1006–1014 (2017).
44. J. Barna, P. Csermely, T. Vellai, Roles of heat shock factor 1 beyond the heat shock response. *Cell. Mol. Life Sci.* **75**, 2897–2916 (2018).
45. D. P. Jones, H. Sies, The redox code. *Antioxid. Redox Signal.* **23**, 734–746 (2015).
46. R. Eferl, E. F. Wagner, AP-1: A double-edged sword in tumorigenesis. *Nat. Rev. Cancer* **3**, 859–868 (2003).
47. L. Z. Zhou, A. P. Johnson, T. A. Rando, NFκB and AP-1 mediate transcriptional responses to oxidative stress in skeletal muscle cells. *Free Radic. Biol. Med.* **31**, 1405–1416 (2001).
48. S. Homma, X. Jin, G. Wang, N. Tu, J. Min, N. Yanasak, N. F. Mivechi, Demyelination, astrogliosis, and accumulation of ubiquitinated proteins, hallmarks of CNS disease in *hsf1*-deficient mice. *J. Neurosci.* **27**, 7974–7986 (2007).
49. R. Kandel, J. Jung, S. Neal, Proteotoxic stress and the ubiquitin proteasome system. *Semin. Cell Dev. Biol.* **156**, 107–120 (2024).
50. P. van Bergeijk, C. C. Hoogenraad, L. C. Kapitein, Right time, right place: Probing the functions of organelle positioning. *Trends Cell Biol.* **26**, 121–134 (2016).
51. L. A. Banaszynski, C. W. Liu, T. J. Wandless, Characterization of the FKBP.rapamycin.FRB ternary complex. *J. Am. Chem. Soc.* **127**, 4715–4721 (2005).
52. J. Radons, The human HSP70 family of chaperones: Where do we stand? *Cell Stress Chaperones* **21**, 379–404 (2016).
53. B. Song, S. Shen, S. Fu, J. Fu, HSPA6 and its role in cancers and other diseases. *Mol. Biol. Rep.* **49**, 10565–10577 (2022).
54. R. Gozzelino, V. Jeney, M. P. Soares, Mechanisms of cell protection by heme oxygenase-1. *Annu. Rev. Pharmacol. Toxicol.* **50**, 323–354 (2010).
55. C. H. Wong, S. W. Wingett, C. Qian, M. Rose Hunter, J. M. Taliaferro, D. Ross-Thriepland, S. L. Bullock, Genome-scale requirements for dynein-based transport revealed by a high-content arrayed CRISPR screen. *J. Cell Biol.* **223**, e202306048 (2023).
56. C. C. Hoogenraad, P. Wulf, N. Schiefermeier, T. Stepanova, N. Galjart, J. V. Small, F. Grosveld, C. I. de Zeeuw, A. Akhmanova, Bicaudal D induces selective dynein-mediated microtubule minus end-directed transport. *EMBO J.* **22**, 6004–6015 (2003).
57. R. Gopalakrishna, S. Jaken, Protein kinase C signaling and oxidative stress. *Free Radic. Biol. Med.* **28**, 1349–1361 (2000).
58. D. J. Mitchell, K. R. Blasier, E. D. Jeffery, M. W. Ross, A. K. Pullikuth, D. Suo, J. Park, W. R. Smiley, K. W.-H. Lo, J. Shabanowitz, C. D. Deppmann, J. C. Trinidad, D. F. Hunt, A. D. Catling, K. K. Pfister, Trk activation of the ERK1/2 kinase pathway stimulates intermediate chain phosphorylation and recruits cytoplasmic dynein to signaling endosomes for retrograde axonal transport. *J. Neurosci.* **32**, 15495–15510 (2012).
59. F. J. Gao, S. Hebbar, X. A. Gao, M. Alexander, J. P. Pandey, M. D. Walla, W. E. Cotham, S. J. King, D. S. Smith, GSK-3β phosphorylation of cytoplasmic dynein reduces Ndel1 binding to intermediate chains and alters dynein Motility. *Traffic* **16**, 941–961 (2015).
60. J. Scherer, J. Yi, R. B. Vallee, PKA-dependent dynein switching from lysosomes to adenovirus: A novel form of host-virus competition. *J. Cell Biol.* **205**, 163–177 (2014).
61. Y. Naito, N. Asada, M. D. Nguyen, K. Sanada, AMP-activated protein kinase regulates cytoplasmic dynein behavior and contributes to neuronal migration in the developing neocortex. *Development* **147**, dev187310 (2020).
62. N. Gallisà-Suñé, P. Sànchez-Fernàndez-de-Landa, F. Zimmermann, M. Serna, L. Regué, J. Paz, O. Llorca, J. Luders, J. Roig, BICD2 phosphorylation regulates dynein function and centrosome separation in G2 and M. *Nat. Commun.* **14**, 2434 (2023).
63. D. Mori, Y. Yano, K. Toyo-oka, N. Yoshida, M. Yamada, M. Muramatsu, D. Zhang, H. Saya, Y. Y. Toyoshima, K. Kinoshita, A. Wynshaw-Boris, S. Hirotsune, NDEL1 phosphorylation by Aurora-A kinase is essential for centrosomal maturation, separation, and TACC3 recruitment. *Mol. Cell. Biol.* **27**, 352–367 (2007).
64. K. Okada, B. R. Iyer, L. G. Lammers, P. A. Gutierrez, W. Li, S. M. Markus, R. J. McKenney, Conserved roles for the dynein intermediate chain and Ndel1 in assembly and activation of dynein. *Nat. Commun.* **14**, 5833 (2023).
65. S. R. Garrott, J. P. Gillies, A. Siva, S. R. Little, R. El Jbeily, M. E. DeSantis, Ndel1 disfavors dynein-dynactin-asaptor complex formation in two distinct ways. *J. Biol. Chem.* **299**, 104735 (2023).
66. M. Segal, I. Soifer, H. Petzold, J. Howard, M. Elbaum, O. Reiner, Ndel1-derived peptides modulate bidirectional transport of injected beads in the squid giant axon. *Biol. Open* **1**, 220–231 (2012).
67. R. J. McKenney, S. J. Weil, J. Scherer, R. B. Vallee, Mutually exclusive cytoplasmic dynein regulation by NudE-Lis1 and dynactin. *J. Biol. Chem.* **286**, 39615–39622 (2011).
68. S. Wang, S. A. Ketcham, A. Schön, B. Goodman, Y. Wang, J. Yates III, E. Freire, T. A. Schroer, Y. Zheng, Nudel/NudE and Lis1 promote dynein and dynactin interaction in the context of spindle morphogenesis. *Mol. Biol. Cell* **24**, 3522–3533 (2013).
69. E. Zyłkiewicz, M. Kijańska, W. C. Choi, U. Derewenda, Z. S. Derewenda, P. T. Stukenberg, The N-terminal coiled-coil of Ndel1 is a regulated scaffold that recruits LIS1 to dynein. *J. Cell Biol.* **192**, 433–445 (2011).
70. E. Klinman, E. L. Holzbaur, Stress-induced CDK5 activation disrupts axonal transport via Lis1/Ndel1/Dynein. *Cell Rep.* **12**, 462–473 (2015).
71. L. Rao, X. Liu, M. Arnold, K. Okada, R. J. McKenney, K. Stengel, S. Sidoli, F. Berger, A. Gennerich, Adaptor-mediated recruitment of three dyneins to dynactin enhances force generation. *Nat. Cell Biol.* **28**, 480–491 (2026).
72. Q. Rao, J. Yang, P. Chai, S. Markus, K. Zhang, Roles of microtubules and LIS1 in dynein transport machinery assembly. *Nature* **652**, 1384–1392 (2026).
73. C. Gladkova, M. G. Paez-Segala, W. P. Grant, M. Kittisopikul, S. A. Myers, Y. Wang, R. D. Vale, A molecular switch for coordinating kinesin and dynein transport of mitochondrial cargo. *Science* **393**, 601–606 (2026).
74. R. Desai, D. A. East, L. Hardy, D. Faccenda, M. Rigon, J. Crosby, M. S. Alvarez, A. Singh, M. Mainenti, L. K. Hussey, R. Bentham, G. Szabadkai, V. Zappulli, G. K. Dhoot, L. E. Romano, D. Xia, I. Coppens, A. Hamacher-Brady, J. P. Chapple, R. Abeti, R. A. Fleck, G. Vizcay-Barrena, K. Smith, M. Campanella, Mitochondria form contact sites with the nucleus to couple prosurvival retrograde response. *Sci. Adv.* **6**, eabc9955 (2020).
75. P. Mayinger, Signaling at the Golgi. *Cold Spring Harb. Perspect. Biol.* **3**, a005314 (2011).
76. A. Meichsner, V. Bader, K. F. Winklhofer, Mitochondria as sources and targets of cellular signaling. *Mol. Cell* **86**, 503–521 (2026).
77. M. P. Smith, H. R. Ferguson, J. Ferguson, E. Zindy, K. M. Kowalczyk, T. Kedward, C. Bates, J. Parsons, J. Watson, S. Chandler, P. Fullwood, S. Warwood, D. Knight, R. B. Clarke, C. Francavilla, Reciprocal priming between receptor tyrosine kinases at recycling endosomes orchestrates cellular signalling outputs. *EMBO J.* **40**, e107182 (2021).
78. I. Andreu, I. Granero-Moya, N. R. Chahare, K. Clein, M. Molina-Jordan, A. E. M. Beedle, A. Elosegui-Artola, J. F. Abenza, L. Rossetti, X. Trepat, B. Raveh, P. Roca-Cusachs, Mechanical force application to the nucleus regulates nucleocytoplasmic transport. *Nat. Cell Biol.* **24**, 896–905 (2022).
79. C. Uhler, G. V. Shivashankar, Regulation of genome organization and gene expression by nuclear mechanotransduction. *Nat. Rev. Mol. Cell Biol.* **18**, 717–727 (2017).
80. M. Batty, M. R. Bennett, E. Yu, The role of oxidative stress in atherosclerosis. *Cells* **11**, 3843 (2022).
81. X. Liang, J. Weng, Z. You, Y. Wang, J. Wen, Z. Xia, S. Huang, P. Luo, Q. Cheng, Oxidative stress in cancer: From tumor and microenvironment remodeling to therapeutic frontiers. *Mol. Cancer* **24**, 219 (2025).
82. J. S. Bhatti, A. Sehrawat, J. Mishra, I. S. Sidhu, U. Navik, N. Khullar, S. Kumar, G. K. Bhatti, P. H. Reddy, Oxidative stress in the pathophysiology of type 2 diabetes and related complications: Current therapeutics strategies and future perspectives. *Free Radic. Biol. Med.* **184**, 114–134 (2022).
83. P. Muro, L. Zhang, S. Li, Z. Zhao, T. Jin, F. Mao, Z. Mao, The emerging role of oxidative stress in inflammatory bowel disease. *Front. Endocrinol.* **15**, 1390351 (2024).
84. H. J. Forman, H. Zhang, Targeting oxidative stress in disease: Promise and limitations of antioxidant therapy. *Nat. Rev. Drug Discov.* **20**, 689–709 (2021).
85. A. Kupfer, D. Louvard, S. J. Singer, Polarization of the Golgi apparatus and the microtubule-organizing center in cultured fibroblasts at the edge of an experimental wound. *Proc. Natl. Acad. Sci. U.S.A.* **79**, 2603–2607 (1982).
86. A. F. Palazzo, H. L. Joseph, Y. J. Chen, D. L. Dujardin, A. S. Alberts, K. K. Pfister, R. B. Vallee, G. G. Gundersen, Cdc42, dynein, and dynactin regulate MTOC reorientation independent of Rho-regulated microtubule stabilization. *Curr. Biol.* **11**, 1536–1541 (2001).
87. G. Xiang, Z. Liu, Z. Yuan, Z. Ying, Y. Ding, D. Lin, H. Qin, S. Dong, S. Zhou, H. Yuan, W. Xie, Z. Zheng, Y. Chen, L. Li, Q. Long, L. Yang, Y. Wu, K. Chen, F. Bao, Y. Huang, W. Li, J. Wang, Y. Liu, D. Qin, X. Liu, Perinuclear mitochondrial clustering for mesenchymal-to-epithelial transition in pluripotency induction. *Stem Cell Rep.* **20**, 102474 (2025).
88. V. Madan, L. Albacete-Albacete, L. Jin, P. Scaturro, J. L. Watson, N. Muschalik, F. Begum, J. Boulanger, K. Bauer, M. A. Kiebler, E. Derivery, S. L. Bullock, HEATR5B associates with dynein-dynactin and promotes motility of AP1-bound endosomal membranes. *EMBO J.* **42**, e114473 (2023).
89. N. Sato, V. S. Rosa, A. Makhlouf, H. Kretzmer, A. Sampath Kumar, S. Grosswendt, A. L. Mattei, O. Courbot, S. Wolf, J. Boulanger, F. Langevin, M. Wiacek, D. Karpinski, A. Elosegui-Artola, A. Meissner, M. Zernicka-Goetz, M. N. Shahbazi, Basal delamination during mouse gastrulation primes pluripotent cells for differentiation. *Dev. Cell* **59**, 1252–1268.e13 (2024).
90. S. R. Edwards, T. J. Wandless, The rapamycin-binding domain of the protein kinase mammalian target of rapamycin is a destabilizing domain. *J. Biol. Chem.* **282**, 13395–13401 (2007).
91. S. Dunst, T. Kazimiers, F. von Zadow, H. Jambor, A. Sagner, B. Brankatschk, A. Mahmoud, S. Spannl, P. Tomancak, S. Eaton, M. Brankatschk, Endogenously tagged rab proteins: A resource to study membrane trafficking in *Drosophila*. *Dev. Cell* **33**, 351–365 (2015).
92. J. Schindelin, I. Arganda-Carreras, E. Frise, V. Kaynig, M. Longair, T. Pietzsch, S. Preibisch, C. Rueden, S. Saalfeld, B. Schmid, J. Y. Tinevez, D. J. White, V. Hartenstein, K. Eliceiri, P. Tomancak, A. Cardona, Fiji: An open-source platform for biological-image analysis. *Nat. Methods* **9**, 676–682 (2012).

Acknowledgments: We thank the Bullock group and other members of the LMB community for support and advice. We are grateful for the contributions of Y. Andrés Jeske, R. Kazi, S. M. Sundaram, V. de Souza Rosa, S. Wingett, J. Boulanger, C. Franco, F. Begum, K. C. Liu,

E. Derivery, P. A. Penttilä, and the Light Microscopy Facility. We also thank M. Gaspar, F. Wollerton, and C. Overed-Sayer (AstraZeneca) for encouragement and helpful input. **Funding:** This work was supported by the following: European Molecular Biology Organization (M.N.S.), UK Research and Innovation (M.N.S.), UK Research and Innovation (S.L.B.), Engineering and Physical Sciences Research Council (M.N.S.), LMB-AstraZeneca Blue Sky award (L.A.-A.), and LMB-AstraZeneca Blue Sky award (S.L.B.). **Author contributions:** Conceptualization: L.A.-A. and S.L.B. Formal analysis: L.A.-A. Funding acquisition: M.N.S., L.A.-A., and S.L.B. Investigation: L.A.-A., L.J., and N.S. Methodology: L.A.-A. Supervision: M.N.S. and S.L.B. **Competing interests:** The authors declare that they have no competing interests. **Data, code, and materials availability:** All data and code needed to evaluate and reproduce the results in the paper are present in the paper and/or the Supplementary Materials. Mass spectrometry data are available at PRIDE with identifier PXD075576 (www.ebi.ac.uk/pride/archive/projects/PXD075576). RNA-seq data are available at Gene Expression Omnibus with identifier GSE324663 (www.ncbi.nlm.nih.gov/geo/query/acc.cgi?acc=GSE324663). Summaries of mass spectrometry and RNA-seq results are provided as datasets S1 and S2, respectively. Materials generated in this study are available from the corresponding authors upon request (L.A.-A., lalbacete@mrclmb.ac.uk; S.L.B., sbullock@mrclmb.ac.uk).

Submitted 30 March 2026
Accepted 13 October 2026
Published 18 November 2026
10.1126/sciadv.aeh6455